

24 **Abstract**

25 Rainfall frequency analysis, which is an important tool in hydrologic engineering, has been
26 traditionally performed using information from gauge observations. This approach has proven to
27 be a useful tool in planning and design for the regions where sufficient observational data are
28 available. However, in many parts of the world where ground-based observations are sparse and
29 limited in length, the effectiveness of statistical methods for such applications is highly limited.
30 The sparse gauge networks over those regions, especially over remote areas and high-elevation
31 regions, cannot represent the spatiotemporal variability of extreme rainfall events and hence
32 preclude developing depth-duration-frequency curves (DDF) for rainfall frequency analysis.

33 In this study, the PERSIANN-CDR dataset is used to propose a mechanism, by which satellite
34 precipitation information could be used for rainfall frequency analysis and development of DDF
35 curves. In the proposed framework, we first adjust the extreme precipitation time series
36 estimated by PERSIANN-CDR using an elevation-based correction function, then use the
37 adjusted dataset to develop DDF curves. As a proof of concept, we have implemented our
38 proposed approach in 20 river basins in the United States with different climatic conditions and
39 elevations. Bias adjustment results indicate that the correction model can significantly reduce the
40 biases in PERSIANN-CDR estimates of annual maximum series, especially for high elevation
41 regions. Comparison of the extracted DDF curves from both the original and adjusted
42 PERSIANN-CDR data with the reported DDF curves from NOAA Atlas 14 shows that the
43 extreme percentiles from the corrected PERSIANN-CDR are consistently closer to the gauge-
44 based estimates at the tested basins. The median relative errors of the frequency estimates at the
45 studied basins were less than 20% in most cases. Our proposed framework has the potential for
46 constructing DDF curves for regions with limited or sparse gauge-based observations using

47 remotely sensed precipitation information, and the spatiotemporal resolution of the adjusted
48 PERSIANN-CDR data provides valuable information for various applications in remote and high
49 elevation areas.

50

51 Keywords: Rainfall Frequency Analysis, Extreme Precipitation, PERSIANN-CDR, High
52 Elevation, Depth-Duration-Frequency Curves

53 **1. Introduction**

54 Rainfall Frequency Analysis (RFA) is an important tool in hydrologic engineering (Bonnin et al.
55 2006, Hosking and Wallis 2005, Stedinger 1993). Depth-Duration-Frequency (DDF) curves,
56 which link extreme rainfall depths to their probability of occurrence, are based on time series of
57 extreme rainfall with different durations fitted with probability distribution functions. RFA has
58 been traditionally performed using information from rain gauges. This approach has proven to be
59 a useful tool in planning and design for regions where observational data is relatively abundant
60 such as the United States or Europe. However, many parts of the world, particularly the
61 developing countries, do not have that advantage. In many developing countries, gauge
62 observation networks over remote and mountainous regions are still sparse and limited in terms
63 of duration.

64 With advances in tools and techniques for precipitation measurement using remotely sensed
65 information, investigation of rainfall characteristics over remote and mountainous regions with
66 limited gauge observations has become possible. In an effort to produce long and consistent
67 climate records based on satellite observations, National Oceanic and Atmospheric Association
68 (NOAA) under the Climate Data Record (CDR) program, in cooperation with the University of
69 California, Irvine, developed a satellite precipitation product named the Precipitation Estimation
70 from Remotely Sensed Information and Artificial Neural Networks-Climate Data Record
71 (PERSIANN-CDR) (Ashouri et al. 2015). PERSIANN-CDR provides near-global (60°N to 60°S
72 latitude and 0° to 360° longitude) precipitation information with 0.25° spatial and daily temporal
73 resolution from 1983 to the present. Given its relatively high spatial resolution and long record,
74 PERSIANN-CDR is a unique dataset for studying extreme precipitations and performing rainfall

75 frequency analysis. The length of the PERSIANN-CDR dataset (34+ years) is particularly
76 valuable for parts of the world that lack the gauge information for rainfall frequency analysis.
77 In recent years, several efforts have been made to develop DDF curves by employing remotely
78 sensed precipitation information from weather radars and earth observing satellites (Eldardiry et
79 al. 2015, Marra and Morin 2015, Overeem et al. 2008, Overeem et al. 2009, Wright et al. 2013).
80 For instance, Overeem et al. (2009) used an 11-year gauge-adjusted radar-rainfall dataset and
81 performed a regional frequency analysis to extract DDF curves for the Netherlands. They found
82 that radar data, despite being useful for real-time rainfall analysis, still suffer from serious
83 limitations, such as significant errors in extreme rainfall estimates and shortness of data, that
84 limit their usefulness for RFA. Thus, the application of radar data for rainfall frequency analysis
85 is hampered by: (1) its relatively short length of record which leads to sampling issues during
86 distribution fitting process and results in larger uncertainties of the frequency estimates
87 especially for longer durations; and, (2) estimation uncertainties and heterogeneities due to the
88 continuous development of radar quantitative precipitation estimation (QPE) instruments and
89 methods (Allen and DeGaetano 2005, Lombardo et al. 2006). Eldardiry et al. (2015) quantified
90 the effects of each of these sources of uncertainty and attributed much of the quantile estimation
91 uncertainty to the length of the dataset. However, the conditional bias intrinsic to the radar
92 dataset was the main reason for the observed systematic underestimations in the rainfall
93 frequency estimates. As compared to rain gauges and radar network, satellite QPE is able to
94 provide global coverage and has been employed in a number of studies for rainfall frequency
95 analysis (Awadallah et al. 2011, Endreny and Imbeah 2009, Marra et al. 2017, Zhou et al. 2015).
96 Yet, similar to radars, the application satellite QPEs for RFA is undermined by the data length
97 issues and estimation uncertainties associated with each of the precipitation estimation products.

98 Among different remotely sensed precipitation datasets, PERSIANN-CDR is a viable candidate
99 for extreme precipitation analysis given: (1) its high spatial and temporal resolution: when
100 compared with the long-term Global Precipitation Climatology Project (GPCP) (Huffman et al.
101 1997) product which is monthly and 2.5° by 2.5°, PERSIANN-CDR has a higher temporal (daily
102) and spatial resolution (0.25° by 0.25°). The 2.5° spatial and monthly temporal resolution is not
103 capable of capturing the spatial and temporal variability of the extreme precipitations especially
104 over regions with complex topographic conditions, and (2) its long record: PERSIANN-CDR has
105 relatively longer data record (34+ years and continually expanding) in comparison to TRMM
106 3b42 V7 (Huffman et al. 2007) with 20+ years of data, or CMORPH (Joyce et al. 2004) with 16+
107 years of record. Based on these strengths, Gado et al. (2017) employed the PERSIANN-CDR
108 dataset to estimate extreme rainfall quantiles at two homogenous regions in the Western United
109 States. They combined information from the PERSIANN-CDR pixels and nearby gauges in a
110 homogenous region and used an innovative regional frequency analysis method to derive
111 quantile estimates at ungauged locations.

112

113 The primary goal of this research is to evaluate the feasibility of using the PERSIANN-CDR
114 dataset for rainfall frequency analysis by constructing the required DDF curves over regions with
115 limited gauge information or mountainous areas. As a proof of concept, this study has been
116 conducted over the United States, where longer gauge observations with sufficient spatial
117 coverage exist. As some studies have reported, there are biases in the PERSIANN-CDR
118 estimates which necessitate the application of bias-adjustment techniques to improve the
119 accuracy of the PERSIANN-CDR estimates of extreme precipitations (Miao et al. 2015, Duan et
120 al. 2016, Shah and Mishra 2016, Yang et al. 2016, Liu et al. 2017). This study was designed with

121 the following objectives: (1) to propose an elevation-based bias correction model applicable to
122 the PERSIANN-CDR dataset and test over a large number of river basins in the continental
123 United States, and, (2) to demonstrate the usefulness of satellite-based precipitation data in
124 rainfall frequency analysis and use the derived frequency estimates to further verify the
125 effectiveness of the proposed bias-correction model. In the proposed frequency analysis
126 framework, only the PERSIANN-CDR information is used to estimate extreme precipitation
127 quantiles and no information from nearby gauges is incorporated in the development of DDF
128 curves (Gado et al. 2017).

129

130 The rest of this paper is organized as follows: in section 2, a detailed description of gauge and
131 PERSIANN-CDR datasets used in the study is presented, followed by the specifications of the
132 studied basins. The bias-adjustment approach, cross-validation techniques and the frequency
133 analysis procedures pursued in the study are introduced in section 3. Section 4 presents the
134 results and discussion. The main findings and conclusions are summarized in Section 5.

135

136 **2. Data**

137 **2.1. Gauge data**

138 Global Historical Climatology Network (GHCN)-Daily is a quality controlled dataset that is used
139 in this study. This dataset contains comprehensive information of daily summaries of more than
140 40 meteorological variables, including precipitation, temperature, snow depth, wind information,
141 evaporation, etc. recorded by 100,000 land surface stations operated by 20 agencies around the
142 world.

143 In this study, we select 20 basins located in the Eastern and Western United States (Figure 1).
144 The daily rainfall data from rain gauges with 34+ years of observation (1/1/1983-12/31/2015)
145 were downloaded from National Oceanic and Atmospheric Association-National Climatic Data
146 Center (NOAA-NCDC) database (<https://www.ncdc.noaa.gov/ghcnd-data-access>). A brief
147 description of the selected basins with their hydrologic unit codes (HUC) and the number of
148 gauges with 34+ years of data selected for this study are presented in Table 1. The selected
149 basins incorporate a wide range of elevations, from 0 to 3700 m mean sea level, and diverse
150 climatic conditions.

151 <Figure 1 here, please! Thanks!>

152 Figure 1. The geographic location of the selected basins and gauges

153

154 **2.2. PERSIANN-CDR data**

155 PERSIANN-CDR is a retrospective multi-satellite precipitation dataset that provides near-global
156 precipitation information, 60°N-60°S latitude and 0°-360° longitude, at 0.25° spatial resolution
157 (around 25 km) and daily temporal resolution from 1 January 1983 to near present (Ashouri et al.
158 2015). The PERSIANN-CDR dataset was developed by the following steps. In the first step, the
159 PERSIANN algorithm (Hsu et al. 1997) is implemented on the archive of Gridded Satellite
160 (GridSat-B1) Infrared Data (Knapp et al. 2011) from Geostationary Earth Orbiting satellites
161 (GEOs). The model is pre-trained using the National Center for Environmental Prediction
162 (NCEP) Stage IV hourly precipitation data. Then the parameters of the model are kept fixed, and
163 the model is run on the entire historical records of GridSat-B1 to estimate the historical
164 precipitation at 3-hourly resolution. In the next step, the estimated rain-rates are resampled to
165 2.5° spatial resolution and bias-adjusted with GPCP product v2.2 (Adler et al. 2003) to keep it

166 consistent with the GPCP monthly product. Finally, the PERSIANN-CDR dataset is obtained by
167 accumulating the 3-hourly bias adjusted data. In this research, daily PERSIANN-CDR data for
168 the selected basins for the time period of 1/1/1983 to 12/31/2015 was used.

169 Table 1. Summary of the features of the selected basins and gauges

170 <Table 1 here, please! Thanks!>

171 **3. Methodology**

172 **3.1. Model Description**

173 In our proposed bias correction model, we first correct the PERSIANN-CDR estimates of
174 Annual Maxima with gauge data at pixels with available gauge records for the study period. The
175 time series of annual maximum precipitation from both gauge network and PERSIANN-CDR for
176 the corresponding pixels are extracted and sorted in an ascending order. For simplicity, we
177 denote the gauge-based annual maximum series as “GM”, and the PERSIANN-CDR annual
178 maximum series as “PM” hereafter. A zero-intercept regression line is fitted to the scatterplot of
179 GM and PM time series, with the corresponding PM values in the Y-axis and GM values in the
180 X-axis (Figure 2a). The slope of this regression line (called “Correction Factor” or CF hereafter)
181 shows the deviation of PM with respect to ground truth (GM), and it indicates the level of
182 correction required for correcting PM to GM. A CF value larger than one indicates an
183 overestimation of the extreme precipitation by PERSIANN-CDR, and a CF smaller than one
184 implies the underestimation. The larger the deviation of a CF value from the one to one case, the
185 greater the correction required for the PM (Figure 2a).

186 To investigate the orographic characteristics of bias at each basin, the CF values at individual
187 gauges are plotted against the corresponding gauge elevations (Figure 2b). The basin-scale plots
188 are further merged to provide a more comprehensive view of the CF-elevation relationship
189 (Figure 2c). Following the approach mentioned above, an exponential function is fitted to the
190 derived CF-elevation relationship at both individual basin and multi-basins scale as shown in
191 Figure 3c. We construct a correction function based on the CF-elevation relationship derived
192 from 4 Western US basins and test its performance with different cross-validation and validation
193 methods on other basins. The selected basins are San Joaquin River Basin (California), the

194 Willamette River Basin (Oregon), the Upper Columbia River Basin (Washington) and the
195 Colorado Headwaters (Colorado). These basins are selected since they provided bias-elevation
196 information at different elevations and encompassed different climatic conditions, which are
197 representative for building a robust and effective bias correction model applicable to other river
198 bases in the United States. Finally, the correction model based on these four selected river basins
199 is tested on the other 16 basins with different elevation ranges and climatic conditions in the
200 Western and Eastern U. S.

201

202 <Figure 2 here, please! Thanks!>

203 Figure 2. Schematic view of the bias adjustment approach. (a) Estimation of correction factor at a single
204 gauge with annual maximum series (AMS) of gauge and collocated PERSIANN-CDR pixel (b)
205 Correction factor - elevation relationship at single basin scale (each point showing the CF for at a gauge)
206 (c) Correction factor-elevation relationship for multiple basins and the schematic of the fitted exponential
207 function (similar markers showing gauges from the same basin)

208

209 **3.2. Hold-out Cross-Validation**

210 Hold-out cross-validation is implemented to examine how the performance of the correction
211 model is influenced by the number of basins incorporated in the model calibration, and to
212 investigate whether incorporating information from fewer basins could improve the CDR
213 estimates of AMS. The four basins used for training the correction function are divided into two
214 groups. The basins are grouped in a way that information from different elevations and climates
215 are included for each case. A correction function based on the gauge and the PERSIANN-CDR
216 information from the basins in the first group is used to adjust the PM for the basins of the other
217 group, and vice versa. In other words, an exponential regression function is fitted to the CF-

218 elevation relationship from the two basins in the first group and is then used to adjust the AMS
219 from the PERSIANN-CDR dataset for the basins in the second. The effectiveness of the bias-
220 correction functions is assessed using the root mean squared error (RMSE) of the sorted AMS
221 from the adjusted CDR and that of gauge observations, at each of the gauge locations and basins.

222

223 **3.3. Comparison with Gauge Interpolation**

224 Besides comparing the original and corrected PERSIANN-CDR using the approaches mentioned
225 above, we also include a commonly used basin-scale interpolation method for analyzing extreme
226 precipitation over remote and mountainous areas where the gauge network is insufficient or even
227 non-existent (Chen et al. 2008, Doumounia et al. 2014).

228 **3.3.1. Leave-One-Out Cross-Validation**

229 Precipitation intensity at an ungauged location is commonly estimated by interpolating
230 observations from nearby gauges. Performance of the bias-adjusted PERSIANN-CDR dataset in
231 estimating the annual maximum time series at an ungauged location is compared with the
232 estimates from the interpolation method and the original PERSIANN-CDR dataset. At each of
233 the calibration basins, we leave one gauge out of the training phase, and the entire time series of
234 precipitation at this particular gauge location is constructed with the linear interpolation of
235 observations from the remaining gauges. Then, the annual maximum series at the location of the
236 held out gauge is extracted from the interpolated time series. The CF-elevation relationship for
237 the selected calibration basins is derived, and the CF corresponding to the elevation of the
238 removed gauge is used to correct the PM time series at the PERSIANN-CDR pixel over the left-
239 out gauge location. Finally, the interpolation-based annual maximum time series and the
240 corrected PM are compared with the original GM. RMSE is used as the measure of the

241 difference between the calculated time series and the GM. It is worth mentioning that we repeat
242 this procedure for all the gauges at each calibration basin to investigate the robustness of our
243 proposed correction method.

244

245 **3.3.2. K-fold Cross-Validation**

246 The leave-one-out cross-validation approach described in section 3.3 evaluates the performance
247 of the suggested bias-correction approach at a single gauge level. When there is a dense gauge
248 network in a basin, interpolation of available gauge observations may result in better estimates of
249 the AMS at an ungauged site. However, the gauge interpolated estimates could be less reliable
250 when the region has limited or sparse gauge observations. Therefore, to find the breaking point
251 where the corrected PERSIAN-CDR dataset starts to outperform the interpolation-based results,
252 we carry out the k-fold cross-validation.

253 At each of the four basins used in the calibration process, different percentages (i.e., 10, 20, 30,
254 40, 50, 60, 70, and 80%) of gauges are randomly selected and left out. Then, the entire time
255 series of precipitation for the locations of the removed gauges are constructed using the linear
256 interpolation of the daily observations from the remaining gauges. The annual maximum series
257 for the locations of the removed gauges are then extracted from the interpolated time series.
258 Finally, we compare the corrected PM and the interpolation-based annual maximum time series
259 at each gauge location with the GM for that location.

260 Since various combinations of gauges could be selected as test samples, results depend on the
261 distribution of the remaining gauges and the distances between the held out and nearby gauges.
262 To reduce the sensitivity of the results to the selection of gauges, we carry out 30 random
263 selections of the hold-out gauges and consider each selection an independent test. RMSE of the

264 interpolation-based AMS is then compared with RMSE of the corrected PM for the selected
265 gauges in each independent run. The average RMSE of the 30 independent runs is also calculated
266 to have the overall error estimate for different hold-out scenarios (i.e. 10, 20, 30, 40, 50, 60, 70,
267 and 80% of gauges being held out).

268 **3.4. Satellite-based Rainfall Frequency Analysis**

269 National Oceanic and Atmospheric Administration (NOAA) Atlas 14 is a source of rainfall
270 frequency estimates for the United States and its territories. NOAA Atlas 14 provides intensity-
271 duration-frequency (IDF) and depth-duration-frequency (DDF) curves for different regions based
272 on the regional frequency analysis approach (Bonnin et al. 2006). NOAA Atlas 14 IDF and DDF
273 curves were developed using the best fit among different probability distributions, including the
274 3-parameter Generalized Extreme Value (GEV), the Generalized Normal, the Generalized
275 Pareto, the Generalized logistic, the Pearson Type III distributions, the 4-parameter Kappa
276 distribution; and the 5-parameter Wakeby distribution. At 80% of gauges and for sub-daily and
277 daily durations, the GEV gave the best statistics among the 3-parameter distributions and its
278 performance was comparable to that of 4 and 5 parameter distributions. Thus, the GEV was
279 adopted across all gauges and durations (Bonnin et al. 2006).

280 The GEV distribution was firstly introduced by Jenkinson (1955), and it has been widely used
281 for frequency analysis of extreme precipitation and was demonstrated superior over other
282 probability distribution functions in terms of fitting the annual maxima time series (AMS) (Ben-
283 Zvi 2009, Bougadis and Adamowski 2006, Fowler and Kilsby 2003, Gellens 2002, Norbiato et
284 al. 2007, Villarini et al. 2011). The GEV distribution is a 3-parameter probability distribution
285 that combines three extreme value distributions. The type of the distribution is characterized by
286 the value of the shape parameter (ξ). Negative, zero, and positive values of the shape parameter

287 determines the tail behavior of the distribution as short-tailed (Weibull), light-tailed (Gumbel)
 288 and heavy-tailed (Fréchet), respectively. The GEV cumulative distribution function is given by:

289

$$290 \quad F(x) = \exp \left\{ - \left[1 + \xi \left(\frac{x-\mu}{\sigma} \right) \right]^{\frac{-1}{\xi}} \right\} \text{ for } \xi \neq 0 \quad (1)$$

$$291 \quad F(x) = \exp \left\{ - \exp \left[- \left(\frac{x-\mu}{\sigma} \right) \right] \right\} \text{ for } \xi = 0 \quad (2)$$

292

293 , where ξ , μ , and σ are the shape, location, and scale parameters, respectively.

294 To fit the GEV distribution with the PERSIANN-CDR daily precipitation, we first adjust the
 295 data samples, in which the block maximum series of PERSIANN-CDR for 2-day, 3-day, 4-day,
 296 7-day, 10-day, 20-day, 30-day, 45-day and 60-day durations are corrected with gauge data using
 297 the same approach used for daily precipitation.

298 The GEV distribution is fitted to the annual maxima series of corrected CDR for different
 299 durations using *gevfit* function from the Matlab Statistics and Machine Learning Toolbox
 300 (<https://www.mathworks.com/help/stats/gevfit.html>). Maximum likelihood estimation is used to
 301 estimate the parameters of the GEV distribution and the corresponding confidence intervals
 302 (Embrechts et al. 2013, Kotz and Nadarajah 2000). The return level for each return period and
 303 duration is estimated using the inverse GEV function as in equations (3) and (4):

304

$$305 \quad X_T = \mu - \frac{\sigma}{\xi} \left\{ 1 - \left[-\ln \left(1 - \frac{1}{T} \right) \right]^{-\xi} \right\} \text{ for } \xi \neq 0 \quad (3)$$

$$306 \quad X_T = \mu - \sigma \ln \left[-\ln \left(1 - \frac{1}{T} \right) \right] \text{ for } \xi = 0 \quad (4)$$

307

308 , where X_T is the return level (i.e., the rainfall depth that on average is exceeded once in T years),
309 and $T = 1/(1-F)$ is the return period. Using the return levels at different return periods and annual
310 exceedance probabilities, the DDF curves are generated.

311 NOAA Atlas 14 (Bonnin et al. 2006) provides DDF curves with sub-daily, daily and multi-day
312 durations. The DDFs can be downloaded from the NOAA precipitation frequency data server
313 (<https://hdsc.nws.noaa.gov/hdsc/pfds/>). Since the PERSIANN-CDR dataset gives precipitation
314 estimates at daily time scale, the daily and multi-day durations were considered in generating the
315 DDF curves. To remain consistent with NOAA frequency estimates, precipitation durations
316 considered in this study are 1-day, 2-day, 3-day, 4-day, 7-day, 10-day, 20-day, 30-day, 45-day,
317 and 60-day. It should be noted that the durations considered here do not mean precipitation
318 occurred during the entire period, but the sliding window gives the highest value of precipitation
319 accumulation over the selected period. Lastly, we compare the return levels based on the
320 corrected CDR estimates with that of NOAA Atlas 14 at each duration and return period.

321 **3.5. Uncertainty assessment**

322 The confidence intervals of the return levels from the original and the adjusted PERSIANN-CDR
323 datasets are estimated using a bootstrapping technique. We generate 1000 random samples with
324 replacements from the original and adjust AMS at the target gauge locations. Then, the
325 Maximum Likelihood estimation is used to calculate the parameters of the GEV distributions
326 fitted to each of these random samples. Return levels for different durations are calculated using
327 the inverse GEV function evaluated at different return periods. Finally, the 5th and 95th
328 percentiles of the bootstrapped return levels at each duration and return period are taken as the 90
329 percent confidence intervals.

330 **4. Results and Discussion**

331 **4.1. Training basins**

332 Figure 3 shows the scatterplots of the CDR and gauge AMS and the regression line equation at a
333 number of gauges in the Willamette River Basin in the state of Oregon. In some of the gauge
334 locations (Figures 3a-d, and g-i), the original PERSIANN-CDR has a certain degree of
335 underestimation or overestimation, while in some other gauge locations the PERSIANN-CDR
336 estimates are in good agreement with gauge observations (Figures 3e and 3f).

337 An important note here is that a PERSIANN-CDR pixel has an area about 625 km² which is
338 much larger than the sampling area of a rain gauge. The value of a PERSIANN-CDR pixel
339 represents the average precipitation within that pixel's spatial domain. In fact, even if the
340 PERSIANN-CDR estimate at a pixel is completely accurate, its value tends to be smaller than
341 the subpixel point measurements. In other words, by comparing a PERSIANN-CDR pixel with a
342 point measurement, we are carrying out a "point-area" comparison. Therefore, by adjusting the
343 PERSIANN-CDR pixels with point measurements, we are downscaling PERSIANN-CDR to
344 point resolution. This implies that the adjusted dataset should be regarded as a point estimate,
345 rather than an area estimate. Furthermore, there would be time discrepancies between the
346 PERSIANN-CDR's daily interval, and the gauges' 24-hour intervals. Thus, the correction factor
347 accounts for the influence of both "point-area" and time discrepancy issues.

348 <Figure 3 here, please! Thanks!>

349 Figure 3. Scatterplots of gauge and PERSIANN-CDR AMS and the zero intercept regression lines at
350 sample gauge locations in Willamette River Basin. Station names are written above the scatterplots.

351 At each of the four basins selected to build the correction model (i.e., the San Joaquin River
352 Basin, the Willamette River Basin, the Upper Columbia River Basin, and the Colorado

353 Headwaters), the CF at the basin scale is computed by fitting a zero-intercept regression line to
354 the sorted AMS of all the available gauges and that of collocated CDR pixels(Figure 4). In
355 general, the PERSIANN-CDR estimates of AMS tend to be lower than the AMS from gauge
356 observation, with different levels of underestimation in the different basins. The AMS estimates
357 from the original PERSIANN-CDR dataset show considerable underestimation at Colorado
358 Headwaters and Upper Columbia River Basins with CFs equal to 0.46 and 0.57, respectively.

359 <Figure 4 here, please! Thanks!>

360 Figure 4. CF at basin scale for the selected river basins in the Western United States, including (a) San
361 Joaquin River Basin, (b) Willamette River Basin, (c) Upper Columbia River Basin, and (d) Colorado
362 Headwaters River Basin.

363 The scatterplots of CF and gauge elevation for different basins are shown in Figures 5(a-d). In
364 general, an exponential relationship exists between CFs and elevations at each of the four basins.
365 Furthermore, when merging all the available gauge information from the selected river basins
366 together, a comprehensive view of this relationship is demonstrated (Figure 5e). As we can see
367 from Figure 5e, the CFs become smaller with increasing elevation of the gauges. This reduction
368 in the CFs implies the underestimation of AMS at higher elevations.

369 <Figure 5 here, please! Thanks!>

370 Figure 5. CF and elevation relationship at basin and multi-basin scale for (a) San Joaquin River Basin,
371 (b) Willamette River Basin, (c) Upper Columbia River Basin, (d) Colorado Headwaters River Basin, and
372 (e) merging all gauge information for all the basins

373 Both IR-based (such as PERSIANN family) and Passive Microwave based (such as TMPA
374 (Huffman et al. 2007)) precipitation products have been reported to underestimate precipitation

375 in high elevations (Hashemi et al. 2017). This underestimation has been related to several
376 factors. Satellite-based precipitation products have difficulties in retrieving the solid form of
377 precipitation (snow), which is the prevailing type of precipitation at high elevation regions and in
378 the winter season (Hashemi et al. 2017). Moreover, since IR-based precipitation algorithms rely
379 on the cloud top temperatures, they cannot fully detect the orographic enhancements in the liquid
380 phase of precipitation in regions characterized by complex topographic conditions (Shige et al.
381 2013). In addition to the technical and methodological issues inherent to the satellite
382 precipitation estimation methods, the spatial and temporal inconsistencies between the satellite
383 precipitation estimates and gauge observations at high elevation regions can be related to the
384 poor sampling of gauges (Gebregiorgis and Hossain 2014). For instance, Libertino et al. (2016)
385 observed the lowest agreement in the timing of extreme events recorded by TRMM and gauge
386 observations in sparsely gauged regions. Miao et al. (2015) also reported low spatial and
387 temporal agreement in terms of extreme precipitation statistics between the PERSIANN-CDR
388 estimates and gauge observations in regions with low density of gauges.

389

390 As shown in Figure 5, we fit an exponential function to the scatterplots of CF for each gauge and
391 its corresponding elevation. This function is used to correct the CDR-based AMS at different
392 basins in the Eastern and Western United States. However, since this correction model is based
393 on only a few selected basins, it is necessary to be validated using different cross-validation
394 techniques and then be tested on different basins over the continental United States.

395 **4.2. Hold-out cross-validation results**

396 We first carry out hold-out cross-validation on the four selected river basins, in which a
397 correction function based on CF-elevation relationship is built using the information from two of

398 the river basins, Willamette and Upper Columbia river basins. The model is tested on the other
399 two river basins (the San Joaquin and the Colorado Headwater River Basins), and vice versa.
400 The goal is to examine the effect of limited gauge information and basin selection on the overall
401 performance of the bias-correction approach.

402 The effect of bias-correction on the empirical CDF of the PERSIANN-CDR estimates at each of
403 the calibration basins is shown in Figure 6. At basin scale, the correction method shifts the
404 empirical CDF of the AMS from the original CDR towards the gauge-based empirical CDF. In
405 the Willamette River Basin and the Colorado headwaters River Basin, the corrected CDF is close
406 to that of the observation. In the San Joaquin River Basin, the extreme quantiles from the
407 corrected data are closer to the observation. In the Upper Columbia River basin, the corrected
408 PERSIANN-CDR gives better estimates of the largest extreme values compared to the original
409 PERSIANN-CDR. However, it results in an overestimation of the lower quantiles. This is
410 consistent with the results shown in Figure 4, where the regression-based estimates gave some
411 overestimation for values lower than 55 mm.

412 The statistics of the hold-out cross-validation results at gauge scale are presented in Table 2. In
413 most of the gauge locations (111 out of 127 gauges in different basins), the RMSE of the
414 corrected PERSIANN-CDR is lower than that of the original PERSIANN-CDR. This implies the
415 effectiveness of the proposed bias-adjustment approach in correcting the PM at pixel level even
416 in basins with dense gauge networks. At 16 gauges, however, the correction method tends to
417 deteriorate the original PERSIANN-CDR estimates. Among these gauges, 12 are located in low
418 elevation regions (<550 meters from mean sea level), and more than half of them are associated
419 with elevations less than 200 meters from mean sea level. The Upper Columbia and the
420 Willamette River Basins have a larger portion of these gauges with 7 and 5 unsuccessful

421 corrections, respectively. The poor performance of the corrected CDR at those gauge locations
422 could be partly attributed to the complex topographic conditions of those basins, which pose
423 some challenges for the PERSIANN algorithm to estimate precipitation accurately. However, as
424 compared to the original PERSIANN-CDR, the proposed correction approach works well for the
425 majority of gauges in the hold-out cross-validation cases as shown with the lower RMSE values
426 in Table 2.

427 <Figure 6 here, please! Thanks!>

428 Figure 6. Empirical CDF of the AMS from the gauge observations, the original and the corrected
429 PERSIANN-CDR data at basin scale. (a) San Joaquin River Basin, (b) Willamette River Basin,
430 (c) Upper Columbia River Basin, and (d) Colorado Headwaters River Basin

431

432 In addition, the lower variability of CF at different elevations (Figure 5-e) also implies that the
433 correction model has a lower uncertainty at gauges with higher elevation. Having accurate
434 information about extreme precipitation at high elevation regions is very critical since these
435 regions typically account for a considerable fraction of water resources. However, these regions
436 are often poorly gauged and the gauge networks are not often capable of capturing the
437 spatiotemporal variability of extreme precipitations.

438

439 Table 2. The RMSE(mm) of the original and corrected PERSIANN-CDR data during hold-out
440 cross-validation at different gauge locations and basins

441 <Table 2 here, please! Thanks!>

442 **4.3. Leave-one-out cross-validation**

443 In each basin, one gauge is left out at a time, and the time series of precipitation at that gauge
444 location is constructed using linear interpolation. The annual maximum time series from the
445 gauge interpolation and the corrected PERSIANN-CDR are compared with the gauge
446 observations at the corresponding location (Table 3). As shown in Table 3, the RMSE values
447 from the corrected PERSIANN-CDR are consistently lower than those of the original
448 PERSIANN-CDR for all basins. When compared to the interpolation method, corrected
449 PERSIANN-CDR gives lower RMSE values at the San Joaquin, the Willamette, and the
450 Colorado Headwaters River Basins. At the Upper Columbia River Basin, however, the leave-
451 one-out cross-validation results suggest that gauge interpolation performs better than the
452 corrected PERSIANN-CDR data.

453 It is inferable from the gauge scale results that the correction model outperforms the interpolation
454 method in most cases, even if only one of the gauges at a densely gauged basin is removed from
455 the sample. The interpolation method also produces substantial errors at some gauge locations,
456 particularly those locations where the interpolated gauge is relatively far from its surrounding
457 gauges. It is possible that complex topography leads to different precipitation characteristics
458 between nearby gauges and results in uncertainties in the interpolated precipitation estimates.

459

460 Table 3. The RMSE (mm) from leave one out cross validation using gauge interpolation, original and
461 corrected PERSIANN-CDR data

462 <Table 3 here, please! Thanks!>

463 **4.4. K-fold cross-validation**

464 The leave-one-out cross-validation results in the previous section demonstrate that the
465 interpolation-based estimates of AMS achieved by removing one of the gauges may outperform

466 the PERSIANN-CDR estimates at some gauges in a densely-gauged region (e.g., the Upper
467 Columbia River Basin). In order to find the breakpoint where the corrected PERSIANN-CDR
468 will outperform interpolation-based estimates at a basin scale, the k-fold cross validation is
469 implemented. We randomly separate different fractions of all available gauges (0.1, 0.2..., 0.8 of
470 the gauges) in a basin, and remove the selected gauges from the model training phase. This
471 random selection and removal process is repeated 30 times for each fraction level. Then, the
472 entire precipitation time series at those locations are constructed by the linear interpolation of
473 observations from the remaining gauges in that basin. Then RMSE of AMS estimates from both
474 corrected PERSIANN-CDR and gauge interpolation are computed at the removed gauges.

475 Figure 7 shows the average RMSE values of AMS estimates from the interpolation method (blue
476 line) and the corrected PERSIANN-CDR (red line) for different exclusion ratios in each river
477 basin. The horizontal axis defines the number of the iteration, and the vertical axis presents the
478 average RMSE value of the AMS estimates on the excluded gauge locations using the corrected
479 PERSIANN-CDR and gauge interpolation. As the fraction of gauges being removed from the
480 entire samples increases, the errors associated with the interpolation method become larger. In
481 contrast, the errors produced with our proposed correction method remain consistently low for
482 different basins over most of the test scenarios (i.e., different percentages of the gauge being
483 removed). Moreover, the interpolation-based estimates result in large errors in some test
484 scenarios and basins. For example, in the San Joaquin River Basin (Figure 7a), substantial errors
485 are observed in different scenarios and over several independent runs.

486 There are several reasons why errors from the interpolation method have large values in some of
487 the iterations. Extreme precipitation events vary substantially in space and time. The annual
488 maximum precipitation at different points of a basin could be results of various extreme events

489 occurring in different times of the year. When interpolating the daily gauge observations in a
490 region for constructing precipitation time series at an ungauged site, heavy precipitation
491 observed at one or more gauge locations could be falsely extended to the locations that were less
492 impacted by the storm. Similarly, by removing some of the gauges from the population, the
493 extreme events impacting those locations may not be represented in the interpolated time series
494 from the remaining sample and as a result the extreme event at that location would be missed.
495 Both of these cases may result in considerable errors in the annual maximum series estimated
496 from the interpolation method. Other factors that contribute to the significant interpolation errors
497 include long distance of sample gauges from the target locations, substantial elevation
498 differences between the target locations and sample gauges, and the inability of the sample
499 gauges to demonstrate the spatiotemporal variability of rainfall at target locations.

500 The overall errors from the corrected PERSIANN-CDR and the interpolation method at different
501 exclusion ratios and basins are shown in Figure 8. As the portion of gauges being left out
502 increases, the RMSE produced by the interpolation method increases for all the basins, while the
503 proposed correction method for PERSIANN-CDR shows stable errors over different ratios and
504 basins with respect to the AMS results. In the San Joaquin River Basin (Figure 8a), the
505 Willamette River Basin (Figure 8b), and the Colorado Headwaters River Basin (Figure 8d), the
506 corrected PERSIANN-CDR yields lower RMSE values than the gauge interpolation method
507 throughout different ratios, suggesting the effectiveness of the proposed correction approach. In
508 the Upper Columbia River Basin, the gauge interpolation method results in better estimates of
509 the AMS at the ratios up to 30%. However, beyond the 30% threshold, the corrected
510 PERSIANN-CDR produces more accurate estimates of the AMS. Therefore, 30% of total gauges
511 is the breakpoint for the Upper Columbia River Basin in the context of interpolating point gauge

512 information to spatial estimates. By comparing the statistics of corrected PERSIANN-CDR and
513 the traditional interpolation method, it is observed that the proposed correction model generates
514 more accurate estimates of the AMS than does the linear interpolation method. The superiority of
515 the proposed bias-correction method becomes increasingly evident as the gauges become sparser.

516 <Figure 7 here, please! Thanks!>

517 Figure 7. Average RMSE of AMS estimates from corrected PERSIANN-CDR (red lines) and
518 interpolation by k-fold cross-validation (blue lines) for different exclusion ratios at: (a) the San Joaquin
519 River Basin, (b) the Willamette River Basin, (c) the Upper Columbia River Basin, and (d) the Colorado
520 Headwaters River Basin

521 <Figure 8 here, please! Thanks!>

522 Figure 8. Overall RMSE of AMS estimates from corrected PERSIANN-CDR (solid line) and
523 interpolation (dashed line) at different basins, including (a) the San Joaquin River Basin, (b) the
524 Willamette River Basin, (c) the Upper Columbia River Basin, and (d) the Colorado Headwaters River
525 Basin.

526 **4.5. Validation on the Continental U.S.**

527 In previous sections, we demonstrated the effectiveness and robustness of the proposed
528 correction model on the four representative river basins in the western U.S. In this section, we
529 extensively validate the correction model on 16 additional river basins with different climates
530 and topographic conditions across the continental United States (Table 1). The selected basins
531 for validation cover all the climate classes available in the United States based on the Köppen-
532 Geiger climate classification system. In addition, these basins cover a broad range of elevations,
533 from low-lying regions in the state of Florida to high elevation regions in the state of Utah. These
534 basins are also associated with various dominant precipitation mechanisms (such as convective,
535 orographic, and cyclonic) which could influence the performance of the satellite-based
536 precipitation products (Hong et al. 2007, Liu and Zipser 2009).

537 Table 4 presents the errors in AMS estimates from the original and the corrected PERSIANN-
538 CDR data on the tested river basins. According to Table 4, in 15 out of the 16 basins, the
539 correction model results in lower RMSE values compared to the original PERSIANN-CDR data.
540 Significant improvements are observed at high elevation regions such as Dirty Devil, Rio
541 Grande, and Upper Yellowstone river basins with 78.7 %, 72.3 %, 71.6% reduction in the RMSE
542 of AMS, respectively. Also, the correction model considerably decreases the errors in the AMS
543 estimates at mid-elevation regions, such as Mississippi headwaters, Upper Mississippi-Iowa, and
544 Upper Tennessee River basins (Table 4). Among the low elevation regions, Nueces-
545 Southwestern Texas Coastal and Trinity River basins were quite successful with respect to the
546 error reduction by the correction model. However, Pascagoula River Basin is less successful
547 (7.3% decrease in RMSE) and South Florida River Basin fails to improve (29.7% increase in
548 RMSE). Both of these basins are located in the South Atlantic Gulf region, which is

549 characterized by warm convective precipitation mechanisms. As a result of these convective
550 systems, satellite precipitation products often fail to provide accurate estimates at these regions,
551 as we see from the performance of raw data shown in Table 4. Both the Pascagoula and the
552 South Florida river basins have high initial errors compared to the other river basins. Since the
553 model is trained using the information from four river basins in the western United States with
554 different hydroclimatic conditions, it is reasonable for it to not perform as well under temperate
555 and tropical climatic conditions and for extremes caused by warm convective systems.

556

557 Table 4. Bias-correction results in selected basins over the United States

558 <Table 4 here, please! Thanks!>

559 Generally, satellite precipitation estimation algorithms perform poorly in estimating precipitation
560 from shallow and warm convective clouds (Hong et al. 2007, Kubota et al. 2009, Liu and Zipser
561 2009, Sorooshian et al. 2002). One reason behind this poor performance is that these algorithms
562 relate heavy precipitations to deep convective clouds and subsequently underestimate heavy
563 precipitations associated with shallow warm clouds (Hong et al. 2007, Liu and Zipser 2009).
564 Moreover, IR-based methods such as PERSIANN are based on cloud top temperature thresholds
565 that are sometimes too cold for warm orographic clouds (Adler et al. 2003, Dinku et al. 2008).
566 Finally, due to the contamination by the cold anvil cirrus clouds, IR-based precipitation estimates
567 typically display 1-3hr phase shift compared to the maximum diurnal precipitation. These phase
568 shifts influence the performance of IR-based methods in regions dominated by warm convective
569 clouds (Sorooshian et al. 2002).

570 **4.6. Multiday Annual Maximum Series**

571 In Figure 9, we present the scatterplots of the CF-elevation for multi-day duration AMS at
572 Colorado Headwaters (Figures 9 a-j) as an illustrative example. Figures 9 (a)-(j) suggest there is
573 a similar CF-elevation behavior in multi-day AMS analysis for different durations. Figure 9(k)
574 presents the exponential regression functions fitted to each of the N-day maximum scatterplots.
575 According to Figure 9 (k), as durations increase from 1 day to 60 days, the original PERSIANN-
576 CDR estimates of the AMS become more accurate (i.e., closer to the CF=1 line). This is because
577 the PERSIANN-CDR dataset is bias-adjusted with GPCP dataset (Huffman et al. 1997) at a
578 monthly scale and the values from the two datasets become closer to each other at longer
579 durations. Therefore, at 30-days or 60-days analysis, the AMS estimates should be close to gauge
580 observation. Although PERSIANN-CDR and gauge information are adjusted at a monthly scale,
581 the monthly coefficients are applied to daily estimates (Ashouri et al. 2015). Therefore, the sub-
582 monthly or daily estimates may not be compatible with gauge observations at the corresponding
583 scale. Furthermore, the GPCP is a gauge interpolated dataset which its pixel values are
584 essentially the average values of gauge observations within the large grid boundary. However,
585 here we compare the PERSIANN-CDR estimates in pixel scale with the collocated gauge values
586 which could differ substantially from the corresponding GPCP pixel values.

587 <Figure 9 here, please! Thanks!>

588 Figure 9. Scatterplots of CF-elevation for different durations(a-f) and the exponential regression fitted to
589 the CF-elevation data for different durations(k) at Colorado Headwaters Basin

590 **4.7. Depth-Duration-Frequency Curves**

591 Figure 10 shows the DDF curves derived from the adjusted CDR data, the frequency estimates
592 from NOAA Atlas 14, and the 90% confidence intervals for a gauge location in Dirty Devil basin

593 in the state of Utah (USC00420849). We present return levels for daily and multi-day durations
594 given the daily resolution of the PERSIANN-CDR dataset. As shown in Figure 10, the
595 frequency estimates from the original PERSIANN-CDR data are outside the 90% confidence
596 intervals of the NOAA Atlas 14 which suggests the necessity of bias adjustment prior to
597 employing the data for frequency analysis. On the other hand, DDFs from the adjusted
598 PERSIANN-CDR data are well within the 90% confidence intervals of the NOAA Atlas 14
599 DDFs. In most cases, the frequency estimates from the adjusted PERSIANN-CDR are very close
600 to the NOAA Atlas 14 estimates which are calculated by incorporating a larger number of
601 gauges and longer records of data for frequency estimation. Larger deviations from the gauge-
602 based estimates are observed at longer return periods, and there is no clear trend in terms of
603 overestimation or underestimation with respect to duration.

604 As shown in Figure 10, the confidence intervals from the gauge-based and satellite-based DDFs
605 become larger as the return periods increase. This higher uncertainty is because of the lower
606 sample size at the tails of the distributions. Furthermore, the confidence intervals from the
607 original and the adjusted PERSIANN-CDR datasets are relatively comparable given the similar
608 lengths of the two datasets. However, the uncertainty bounds from the satellite-based DDFs are
609 larger than those from the NOAA Atlas 14. One reason behind these larger confidence intervals
610 is the shortness of the PERSIANN-CDR dataset when compared to the gauge information used
611 for the development of NOAA Atlas 14 DDFs. Another reason is the difference between the
612 frequency analysis method implemented here and the method employed in the development of
613 NOAA Atlas 14. NOAA uses the regional frequency analysis based on L-moments to estimate
614 the frequency and intensity of extremes (Hosking and Wallis 2005). The regional frequency
615 analysis method is used in Atlas 14 in order to relieve the uncertainties arising from a low

616 sample size (limited years of observations) during the GEV parameter estimation process.
617 Although the regional frequency analysis method gives frequency estimates with lower
618 uncertainties, it comes with the assumption of regional homogeneity in extreme rainfall
619 characteristics which is not always a valid assumption. Here, the frequency analysis methods and
620 uncertainties of the frequency estimates are outside of the scope of this study, and the DDF
621 curves and their error analyses are the proof of concept.

622 <Figure 10 here, please! Thanks!>

623 Figure 10. Frequency estimates from corrected PERSIANN-CDR, original PERSIANN-CDR and
624 NOAA Atlas 14 with 90% Confidence intervals at gauge USC00420849 in Dirty Devil basin, UT. The
625 red vertical bars, blue vertical bars, and gray shaded area show the 90% Confidence intervals from
626 corrected PERSIANN-CDR, original PERSIANN-CDR and NOAA Atlas 14, respectively.

627

628 As seen in Figure 10, DDFs from the original PERSIANN-CDR suggest underestimation of the
629 extreme precipitation quantiles for different durations. This is expected given the spatial
630 resolution of this dataset. In fact, when considering the remotely sensed precipitation
631 information, we should be aware that the pixel value represents a spatial average of precipitation
632 within the extent of a pixel. In other words, the pixel value disregards the subpixel variability and
633 even if the PERSIANN-CDR estimate at a pixel is completely accurate, its value tends to be
634 smaller than the collocated point measurements. As a result, the extracted DDFs from a satellite
635 pixel tend to demonstrate lower return intervals (Peleg et al. 2018b), as observed in Figure 10.

636 It is worth noting that the estimated DDF curves are not necessarily based on the liquid-phase
637 precipitations and the extracted AMS may comprise snowfalls as well. This is because
638 PERSIANN-CDR and many other satellite-based precipitation estimation algorithms do not

639 distinguish between precipitation phases. In other words, the annual maximum time series
640 extracted and used here may contain solid-phase precipitation extremes due to snowfalls.
641 Although this study does not differentiate between solid and liquid phases of precipitation in
642 order to obtain purely rain-based DDFs, the current framework can be further modified to
643 incorporate additional observations on solid precipitations. There are two approaches to achieve
644 this goal. One approach for this would be to limit the analysis to warm seasons, but the
645 definitions of warm season vary among various geographic locations. Another approach would
646 be to distinguish snowfall from rainfall, but this would require snowfall and air temperature data
647 that are not available everywhere. Future independent research may improve upon the current
648 study by including such additional information.

649 Figure 11 displays the box plots of RMSE of the return level estimates from the original and
650 corrected CDR for different durations and return periods at collocated PERSIANN-CDR pixels
651 and gauges for different basins in the continental US. The corrected PERSIANN-CDR data was
652 used to obtain frequency estimates at different gauge locations in the selected basins, and the
653 results were compared with those from NOAA Atlas 14. Note that three out of the 16 basins
654 (basins #5, #6 and #15) were located in the Pacific Northwest region and two basins (basins #8
655 and #14) were located in the state of Texas, all of which were not covered by or were being
656 updated in the recent volumes of NOAA Atlas 14. Thus, the frequency estimates were only
657 validated at the remaining 11 basins as shown in Figure 11.

658 According to Figure 11, the RMSE values for return level estimates corresponding to longer
659 return periods are generally higher for both datasets. This is expected as the PERSIANN-CDR
660 dataset is relatively shorter than the gauge information used for the development of NOAA Atlas
661 14. The shorter record will result in smaller samples, higher uncertainties, and larger deviations

662 at the tails of the distribution. Over the tested basins, the frequency estimates from the corrected
663 PERSIANN-CDR data have consistently lower median RMSE values than those from the
664 original PERSIANN-CDR at different return periods. The RMSE values at the basins with higher
665 elevations (such as Central Nevada, or Dirty Devil basins) were relatively lower than these at
666 basins with lower elevations (such as Mississippi Headwaters, or Upper Mississippi-Iowa
667 basins), which implies the suitability of the correction approach for high elevation regions.
668 Furthermore, in most of the basins and at different return periods, the corrected dataset shows
669 lower variability in RMSE of the frequency estimates. Corrected PERSIANN-CDR data also
670 demonstrate superior performance in terms of median RMSE and variability of RMSE values at
671 the gauges within the basins. The only case for which the corrected PERSIANN-CDR results in
672 higher RMSE values at different return periods and durations is the South Florida basin, where it
673 was previously shown that the correction model does not improve the AMS estimates due to the
674 climate and the precipitation mechanism.

675 The relative errors of the frequency estimates are calculated to show the relative magnitude of
676 the return level errors compared to the return levels from NOAA Atlas 14. The relative error here
677 is the difference between the frequency estimates from PERSIANN-CDR (original and bias-
678 adjusted) and NOAA Atlas 14, divided by the value from NOAA Atlas 14. Figure 12
679 demonstrates the absolute value of the relative error for the frequency estimates at different
680 durations and return periods from the corrected and original PERSIANN-CDR data. As shown,
681 the relative errors from the corrected PERSIANN-CDR data have consistently lower median
682 values, as well as, lower variability at different return periods in the tested basins. The median
683 relative errors from the corrected data are less than 20% different from the return levels
684 estimated by NOAA Atlas 14. Similar performance is observed when the relative errors of

685 frequency estimates from the two datasets are compared with respect to the extreme precipitation
686 duration. It is also noted that the corrected PERSIANN-CDR dataset does not show a systematic
687 increase or decrease in the relative errors of the frequency estimates, with respect to the duration.
688 The relative errors of the return level estimates from the original PERSIANN-CDR data tend to
689 decrease with increasing duration. This finding is consistent with our observations in Figure 9
690 that revealed lower errors of the original PERSIANN-CDR data for longer duration extreme
691 events. As with Figure 11, the only case in which the corrected data resulted in higher RMSE
692 values was the South Florida basin where the correction model did not improve the AMS
693 estimates (Section 4.5).

694

695 <Figure 11 here, please! Thanks!>

696 Figure 11. RMSE of corrected(red) and original(blue) PERSIANN-CDR frequency estimates for the
697 selected basins in the continental United States.

698

699 <Figure 11 cont'd here, please! Thanks!>

700 Figure 11. Continued.

701 <Figure 12 here, please! Thanks!>

702 Figure 12. Absolute relative error (%) of return level estimates for different durations from corrected(red)
703 and original(blue) PERSIANN-CDR for the selected basins in the United States.

704 <Figure 12 cont'd here, please! Thanks!>

705 Figure 12. Continued.

706 **5. Summary and Conclusions**

707 In this study, the application of the PERSIANN-CDR dataset for rainfall frequency analysis was
708 investigated. A bias correction model was developed to further correct the PERSIANN-CDR
709 estimates of annual maximum time series at the pixel scale. The proposed correction approach
710 was implemented in two steps: (1) Bias correction factors at limited gauge locations were
711 estimated using linear regression analysis between annual maximum series (AMS) of gauges and
712 collocated pixels; and (2) The correction factors from the limited gauge locations were extended
713 to other regions where gauge data were not available. The correction model was validated at 16
714 basins in the continental United States, covering various climates and elevations. Finally, depth-
715 duration-frequency (DDF) curves were constructed by fitting the Generalized Extreme Value
716 distribution to the AMS from the corrected data and estimating the quantiles of extreme
717 precipitations. Below is a summary of our main findings:

- 718 1. The proposed bias correction approach has been demonstrated effective and robust in
719 improving the accuracy of a remote sensing precipitation estimation product (i.e.,
720 PERSIANN-CDR), especially in high-elevation river basins where gauge or radar
721 networks are either limited or non-existent.
- 722 2. The hold-out cross-validation results indicated that the proposed bias correction model
723 is capable of improving the AMS estimated by the PERSIANN-CDR dataset even in the
724 case that limited gauge information was provided for the model calibration and the
725 approach is generalizable to other locations with similar climates and elevations.
- 726 3. As shown by the leave-one-out cross-validation, the bias adjusted PERSIANN-CDR
727 gave better estimates of the AMS for the ungauged sites at a majority of the basins even
728 though these basins had dense gauge networks.

- 729 4. Results from the k-fold cross-validation method suggested the proposed correction
730 approach performs consistently better than the gauge interpolation method in estimating
731 the AMS at a majority of regions with limited gauge observations. It was observed that
732 the gauge interpolation may sometimes result in significant errors in AMS estimates,
733 especially in regions with complex topography.
- 734 5. The validation results over 16 basins across different climates and elevations indicated
735 that the proposed correction method improves the PERSIANN-CDR estimates of AMS,
736 especially in high elevation regions.
- 737 6. The bias-adjusted PERSIANN-CDR is further applied to derive the return levels for
738 different return periods and durations. The frequency estimates from the corrected
739 PERSIANN-CDR data are compared with those from the original PERSIANN-CDR and
740 NOAA Atlas 14. Results revealed that the frequency estimates from the corrected
741 dataset are consistently closer to the estimates from NOAA Atlas 14. They also lie
742 within the uncertainty bounds of NOAA Atlas 14.

743

744 Thus, the PERSIANN-CDR dataset has the potential for being used in rainfall frequency analysis
745 for the regions with limited ground-based observations. However, despite the promising results,
746 there are still some limitations in this dataset and the proposed correction method for the
747 application of frequency analysis. One of these limitations is the temporal resolution of the
748 PERSIANN-CDR dataset. The daily temporal resolution limits the investigation of extreme
749 events with shorter durations (e.g. 3-hourly or hourly). Another limitation is that the frequency
750 analysis here is conducted at the pixel scale using relatively limited samples. A sample of 33
751 annual maximum values is relatively limited for fitting a 3-parameter distribution. This would

752 result in high uncertainties in estimating the parameters of the distribution and the return levels.
753 One remedy to the sample size problem could be the application of regional frequency analysis
754 methods to increase the sample size by incorporating information from the nearby locations with
755 the same climatic conditions.

756 It is also important to note that given the rising global temperatures, rainfall intensities especially
757 at shorter durations are expected to increase. Therefore, the increase in the global temperature
758 could be used as an added factor to adjust historical design rainfall intensities for the warmer
759 temperatures that lie ahead (Peleg et al. 2018a).

760 This work is part of an ongoing research and the presented approaches and results are intended as
761 a proof of concept. Future research in this area may involve, bringing non-stationarities into the
762 bias-adjustment framework (Tao et al. 2018), including covariates into the bias-adjustment
763 framework which requires advanced optimization techniques (Yang et al. 2017), investigating
764 the hydrological modeling applications of the corrected-PERSIANN-CDR data, and developing
765 DDF curves for ungauged regions or areas not included in the current NOAA Atlas 14.

766

767 **6. Acknowledgments**

768 The financial support of this research is from U.S. Department of Energy (DOE Prime Award #
769 DE-IA0000018), California Energy Commission (CEC Award # 300-15-005), MASEEH
770 fellowship, NSF CyberSEES Project (Award CCF-1331915), NOAA/NESDIS/NCDC (Prime
771 award NA09NES4400006 and NCSU CICS and subaward 2009-1380-01), the U.S. Army
772 Research Office (award W911NF-11-1-0422) and the National Key R&D Program of China
773 (Grant No. 2016YFE0102400). Finally, authors would like to thank the anonymous reviewers
774 whose contributions improved the quality of this paper.

775

776 References

777 Adler, R.F., Huffman, G.J., Chang, A., Ferraro, R., Xie, P.-P., Janowiak, J., Rudolf, B., Schneider,
778 U., Curtis, S. and Bolvin, D. (2003) The version-2 global precipitation climatology project (GPCP)
779 monthly precipitation analysis (1979–present). *Journal of Hydrometeorology* 4(6), 1147-1167.

780 Allen, R.J. and DeGaetano, A.T. (2005) Considerations for the use of radar-derived precipitation
781 estimates in determining return intervals for extreme areal precipitation amounts. *Journal of hydrology*
782 315(1), 203-219.

783 Ashouri, H., Hsu, K.-L., Sorooshian, S., Braithwaite, D.K., Knapp, K.R., Cecil, L.D., Nelson, B.R.
784 and Prat, O.P. (2015) PERSIANN-CDR: Daily precipitation climate data record from multisatellite
785 observations for hydrological and climate studies. *Bulletin of the American Meteorological Society* 96(1),
786 69-83.

787 Awadallah, A.G., ElGamal, M., ElMostafa, A. and ElBadry, H. (2011) Developing intensity-
788 duration-frequency curves in scarce data region: an approach using regional analysis and satellite data.
789 *Engineering* 3(03), 215.

790 Ben-Zvi, A. (2009) Rainfall intensity–duration–frequency relationships derived from large partial
791 duration series. *Journal of hydrology* 367(1), 104-114.

792 Bonnin, G.M., Martin, D., Lin, B., Parzybok, T., Yekta, M. and Riley, D. (2006) Precipitation-
793 frequency atlas of the United States. NOAA atlas 14(2).

794 Bougadis, J. and Adamowski, K. (2006) Scaling model of a rainfall intensity-duration-frequency
795 relationship. *Hydrological processes* 20(17), 3747-3757.

796 Chen, M., Shi, W., Xie, P., Silva, V., Kousky, V.E., Wayne Higgins, R. and Janowiak, J.E. (2008)
797 Assessing objective techniques for gauge-based analyses of global daily precipitation. *Journal of*
798 *Geophysical Research: Atmospheres* 113(D4).

799 Dinku, T., Chidzambwa, S., Ceccato, P., Connor, S. and Ropelewski, C. (2008) Validation of
800 high - resolution satellite rainfall products over complex terrain. *International Journal of Remote Sensing*
801 29(14), 4097-4110.

802 Doumounia, A., Gosset, M., Cazenave, F., Kacou, M. and Zougmore, F. (2014) Rainfall monitoring
803 based on microwave links from cellular telecommunication networks: First results from a West African
804 test bed. *Geophysical Research Letters* 41(16), 6016-6022.

805 Duan, Z., Liu, J., Tuo, Y., Chiogna, G. and Disse, M. (2016) Evaluation of eight high spatial
806 resolution gridded precipitation products in Adige Basin (Italy) at multiple temporal and spatial scales.
807 *Science of The Total Environment* 573, 1536-1553.

808 Eldardiry, H., Habib, E. and Zhang, Y. (2015) On the use of radar-based quantitative precipitation
809 estimates for precipitation frequency analysis. *Journal of hydrology* 531, 441-453.

810 Embrechts, P., Klüppelberg, C. and Mikosch, T. (2013) *Modelling extremal events: for insurance*
811 *and finance*, Springer Science & Business Media.

812 Endreny, T.A. and Imbeah, N. (2009) Generating robust rainfall intensity–duration–frequency
813 estimates with short-record satellite data. *Journal of hydrology* 371(1), 182-191.

814 Fowler, H. and Kilsby, C. (2003) A regional frequency analysis of United Kingdom extreme
815 rainfall from 1961 to 2000. *International Journal of Climatology* 23(11), 1313-1334.

816 Gaona, M.F.R., Overeem, A., Leijnse, H. and Uijlenhoet, R. (2015) Measurement and interpolation
817 uncertainties in rainfall maps from cellular communication networks. *Hydrology and Earth System*
818 *Sciences* 19(8), 3571-3584.

819 Gebregiorgis, A. and Hossain, F. (2014) Making satellite precipitation data work for the developing
820 world. *IEEE Geoscience and Remote Sensing Magazine* 2(2), 24-36.

821 Gellens, D. (2002) Combining regional approach and data extension procedure for assessing GEV
822 distribution of extreme precipitation in Belgium. *Journal of hydrology* 268(1), 113-126.

823 Hashemi, H., Nordin, M., Lakshmi, V., Huffman, G.J. and Knight, R. (2017) Bias Correction of
824 Long-Term Satellite Monthly Precipitation Product (TRMM 3B43) over the Conterminous United States.
825 Journal of Hydrometeorology 18(9), 2491-2509.

826 Hawkins, D.M., Basak, S.C. and Mills, D. (2003) Assessing model fit by cross-validation. Journal
827 of chemical information and computer sciences 43(2), 579-586.

828 Hong, Y., Gochis, D., Cheng, J.T., Hsu, K.L. and Sorooshian, S. (2007) Evaluation of PERSIANN-
829 CCS rainfall measurement using the NAME Event Rain Gauge Network. Journal of Hydrometeorology
830 8(3), 469-482.

831 Hosking, J.R.M. and Wallis, J.R. (2005) Regional frequency analysis: an approach based on L-
832 moments, Cambridge University Press.

833 Huffman, G.J., Adler, R.F., Arkin, P., Chang, A., Ferraro, R., Gruber, A., Janowiak, J., McNab, A.,
834 Rudolf, B. and Schneider, U. (1997) The global precipitation climatology project (GPCP) combined
835 precipitation dataset. Bulletin of the American Meteorological Society 78(1), 5-20.

836 Huffman, G.J., Bolvin, D.T., Nelkin, E.J., Wolff, D.B., Adler, R.F., Gu, G., Hong, Y., Bowman,
837 K.P. and Stocker, E.F. (2007) The TRMM multisatellite precipitation analysis (TMPA): Quasi-global,
838 multiyear, combined-sensor precipitation estimates at fine scales. Journal of Hydrometeorology 8(1), 38-
839 55.

840 Jenkinson, A.F. (1955) The Frequency Distribution of the Annual Maximum (or Minimum) Values
841 of Meteorological Elements. Quarterly Journal of the Royal Meteorological Society 81(348), 158-171.

842 Joyce, R.J., Janowiak, J.E., Arkin, P.A. and Xie, P. (2004) CMORPH: A method that produces
843 global precipitation estimates from passive microwave and infrared data at high spatial and temporal
844 resolution. Journal of Hydrometeorology 5(3), 487-503.

845 Kim, J.-H. (2009) Estimating classification error rate: Repeated cross-validation, repeated hold-out
846 and bootstrap. Computational statistics & data analysis 53(11), 3735-3745.

847 Knapp, K.R., Ansari, S., Bain, C.L., Bourassa, M.A., Dickinson, M.J., Funk, C., Helms, C.N.,
848 Hennon, C.C., Holmes, C.D. and Huffman, G.J. (2011) Globally gridded satellite observations for climate
849 studies. *Bulletin of the American Meteorological Society* 92(7), 893-907.

850 Kottek, M., Grieser, J., Beck, C., Rudolf, B. and Rubel, F. (2006) World map of the Köppen-Geiger
851 climate classification updated. *Meteorologische Zeitschrift* 15(3), 259-263.

852 Kotz, S. and Nadarajah, S. (2000) *Extreme value distributions: theory and applications*, World
853 Scientific.

854 Kubota, T., Ushio, T., Shige, S., Kida, S., Kachi, M. and Okamoto, K.i. (2009) Verification of high-
855 resolution satellite-based rainfall estimates around Japan using a gauge-calibrated ground-radar dataset.
856 *Journal of the Meteorological Society of Japan. Ser. II* 87, 203-222.

857 Libertino, A., Sharma, A., Lakshmi, V. and Claps, P. (2016) A global assessment of the timing of
858 extreme rainfall from TRMM and GPM for improving hydrologic design. *Environmental Research*
859 *Letters* 11(5).

860 Liu, C. and Zipser, E.J. (2009) “Warm rain” in the tropics: Seasonal and regional distributions
861 based on 9 yr of TRMM data. *Journal of climate* 22(3), 767-779.

862 Liu, X.M., Yang, T.T., Hsu, K.L., Liu, C.M. and Sorooshian, S. (2017) Evaluating the streamflow
863 simulation capability of PERSIANN-CDR daily rainfall products in two river basins on the Tibetan
864 Plateau. *Hydrology and Earth System Sciences* 21(1), 169-181.

865 Lombardo, F., Napolitano, F., Russo, F., Scialanga, G., Baldini, L. and Gorgucci, E. (2006) Rainfall
866 estimation and ground clutter rejection with dual polarization weather radar. *Advances in Geosciences* 7,
867 127-130.

868 Marra, F. and Morin, E. (2015) Use of radar QPE for the derivation of Intensity-Duration-
869 Frequency curves in a range of climatic regimes. *Journal of hydrology* 531, 427-440.

870 Marra, F., Morin, E., Peleg, N., Mei, Y. and Anagnostou, E.N. (2017) Intensity–duration–frequency
871 curves from remote sensing rainfall estimates: comparing satellite and weather radar over the eastern
872 Mediterranean. *Hydrology and Earth System Sciences* 21(5), 2389.

873 Menne, M.J., Durre, I., Vose, R.S., Gleason, B.E. and Houston, T.G. (2012) An overview of the
874 global historical climatology network-daily database. *Journal of Atmospheric and Oceanic Technology*
875 29(7), 897-910.

876 Miao, C., Ashouri, H., Hsu, K.-L., Sorooshian, S. and Duan, Q. (2015) Evaluation of the
877 PERSIANN-CDR daily rainfall estimates in capturing the behavior of extreme precipitation events over
878 China. *Journal of Hydrometeorology* 16(3), 1387-1396.

879 Norbiato, D., Borga, M., Sangati, M. and Zanon, F. (2007) Regional frequency analysis of extreme
880 precipitation in the eastern Italian Alps and the August 29, 2003 flash flood. *Journal of hydrology* 345(3),
881 149-166.

882 Overeem, A., Buishand, A. and Holleman, I. (2008) Rainfall depth-duration-frequency curves and
883 their uncertainties. *Journal of hydrology* 348(1-2), 124-134.

884 Overeem, A., Buishand, T.A. and Holleman, I. (2009) Extreme rainfall analysis and estimation of
885 depth-duration-frequency curves using weather radar. *Water Resources Research* 45.

886 Peleg, N., Marra, F., Fatichi, S., Molnar, P., Morin, E., Sharma, A. and Burlando, P. (2018a)
887 Intensification of convective rain cells at warmer temperatures observed from high-resolution weather
888 radar data. *Journal of Hydrometeorology* (2018).

889 Peleg, N., Marra, F., Fatichi, S., Paschalis, A., Molnar, P. and Burlando, P. (2018b) Spatial
890 variability of extreme rainfall at radar subpixel scale. *Journal of hydrology* 556, 922-933.

891 Refaeilzadeh, P., Tang, L. and Liu, H. (2009) *Encyclopedia of Database Systems*. Liu, L. and
892 ÖZsu, M.T. (eds), pp. 532-538, Springer US, Boston, MA.

893 Shah, H.L. and Mishra, V. (2016) Uncertainty and Bias in Satellite-Based Precipitation Estimates
894 over Indian Subcontinental Basins: Implications for Real-Time Streamflow Simulation and Flood
895 Prediction*. *Journal of Hydrometeorology* 17(2), 615-636.

896 Shige, S., Kida, S., Ashiwake, H., Kubota, T. and Aonashi, K. (2013) Improvement of TMI rain
897 retrievals in mountainous areas. *Journal of Applied Meteorology and Climatology* 52(1), 242-254.

898 Sorooshian, S., Gao, X., Hsu, K., Maddox, R., Hong, Y., Gupta, H. and Imam, B. (2002) Diurnal
899 variability of tropical rainfall retrieved from combined GOES and TRMM satellite information. *Journal of*
900 *climate* 15(9), 983-1001.

901 Stedinger, J.R. (1993) Frequency analysis of extreme events. *Handbook of hydrology* 18.

902 Tao, Y., Yang, T., Faridzad, M., Jiang, L., He, X. and Zhang, X. (2018) Non - stationary bias
903 correction of monthly CMIP5 temperature projections over China using a residual - based bagging tree
904 model. *International Journal of Climatology* 38(1), 467-482.

905 Villarini, G., Smith, J.A., Baeck, M.L., Vitolo, R., Stephenson, D.B. and Krajewski, W.F. (2011)
906 On the frequency of heavy rainfall for the Midwest of the United States. *Journal of hydrology* 400(1),
907 103-120.

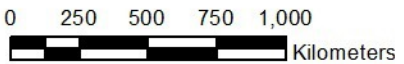
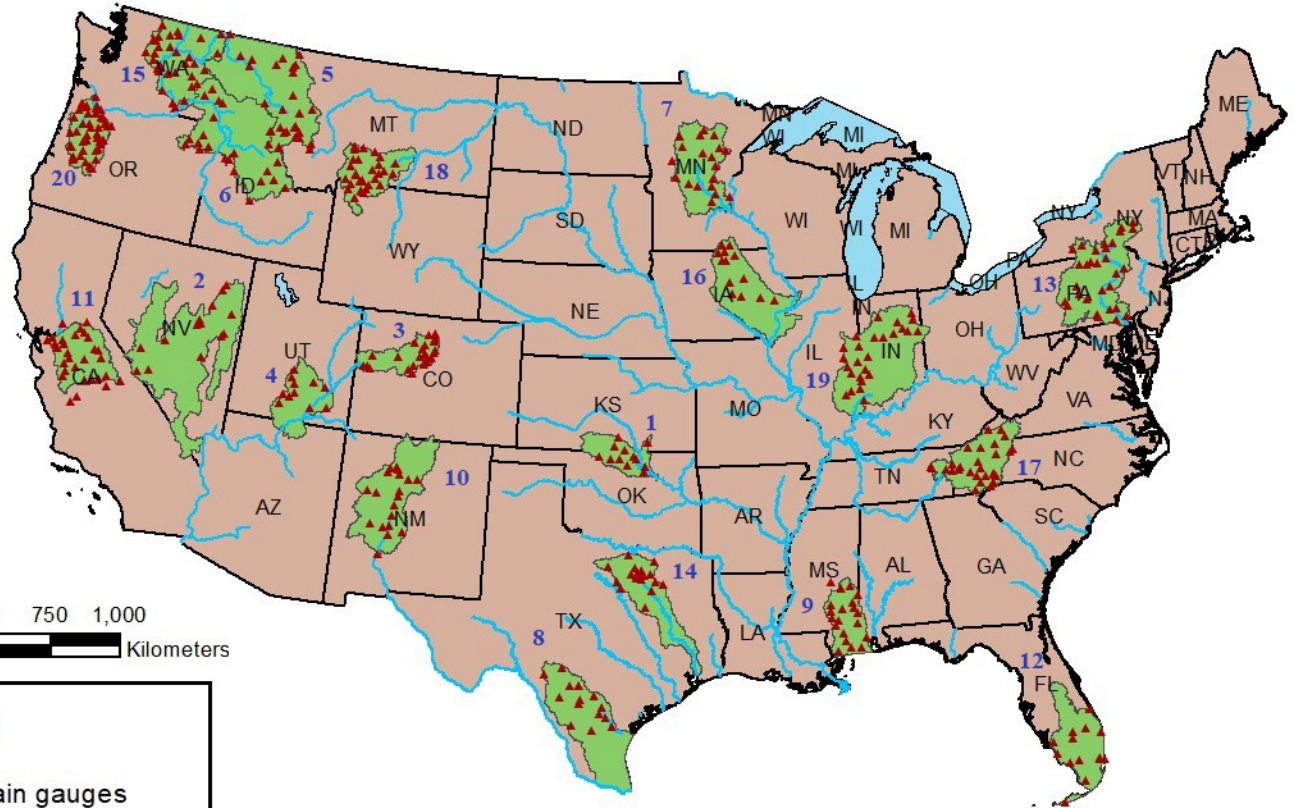
908 Wright, D.B., Smith, J.A., Villarini, G. and Baeck, M.L. (2013) Estimating the frequency of
909 extreme rainfall using weather radar and stochastic storm transposition. *Journal of hydrology* 488, 150-
910 165.

911 Yang, T., Asanjan, A.A., Faridzad, M., Hayatbini, N., Gao, X. and Sorooshian, S. (2017) An
912 enhanced artificial neural network with a shuffled complex evolutionary global optimization with
913 principal component analysis. *Information Sciences* 418, 302-316.




914 Yang, X., Yong, B., Hong, Y., Chen, S. and Zhang, X. (2016) Error analysis of multi-satellite
915 precipitation estimates with an independent raingauge observation network over a medium-sized humid
916 basin. *Hydrological Sciences Journal* 61(10), 1813-1830.

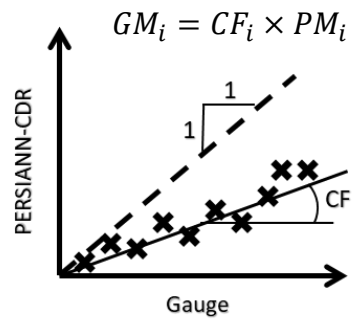
917 Zhou, Y.P., Lau, W.K.M. and Huffman, G.J. (2015) Mapping TRMM TMPA into Average
918 Recurrence Interval for Monitoring Extreme Precipitation Events. *Journal of Applied Meteorology and*
919 *Climatology* 54(5), 979-995.

920



Legend

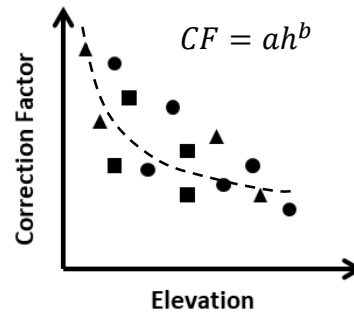
-  Rain gauges
-  Rivers
-  Lakes
-  Selected basins
-  State boundaries



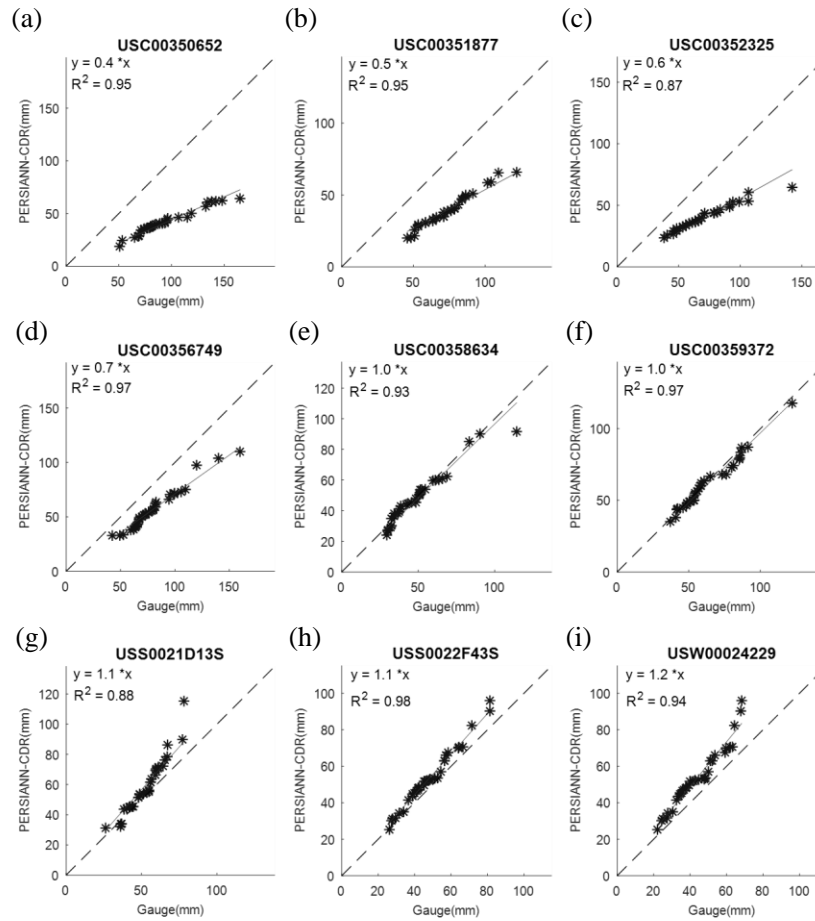
(a)



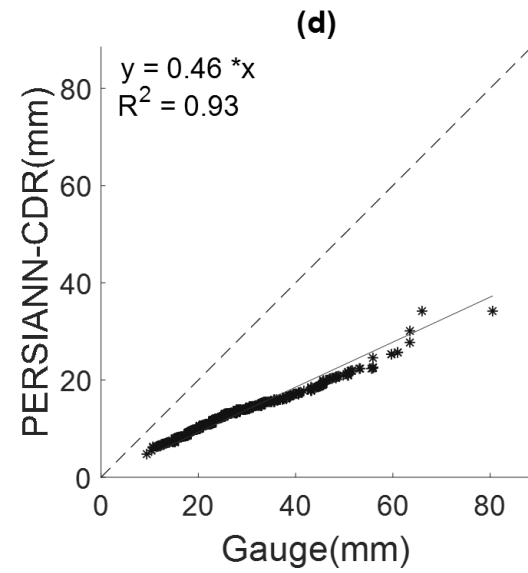
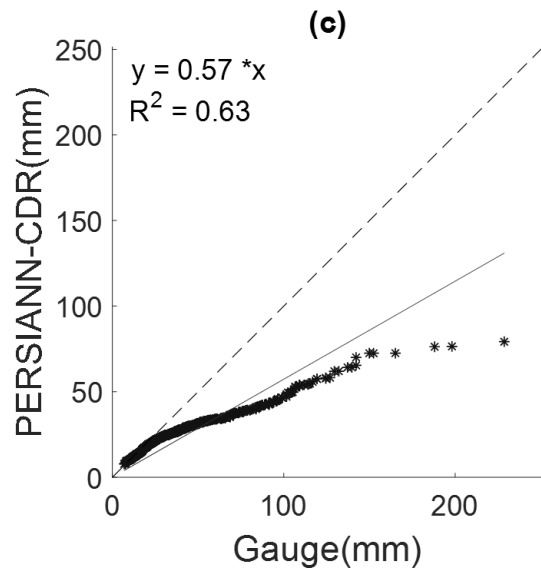
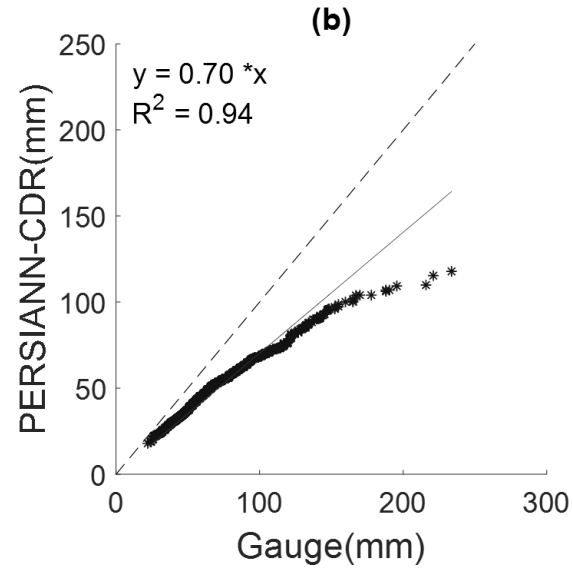
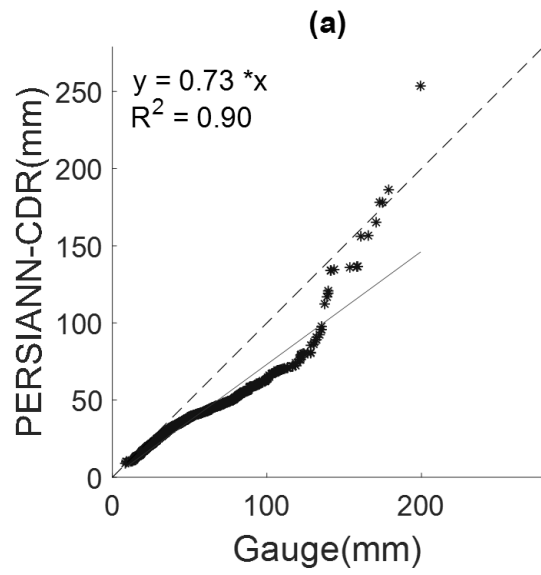
(b)



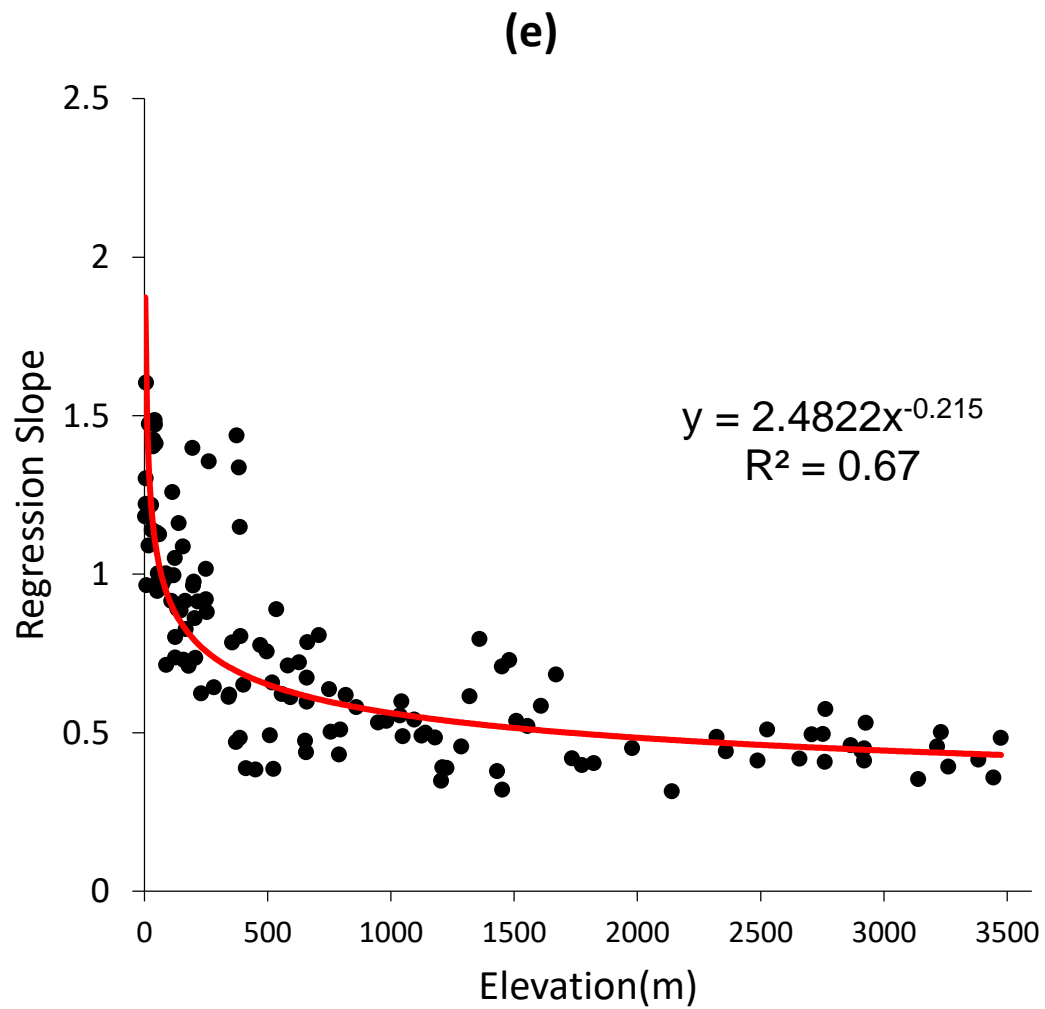
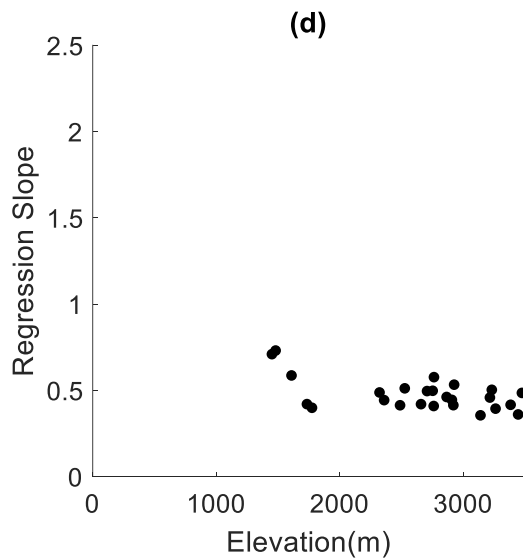
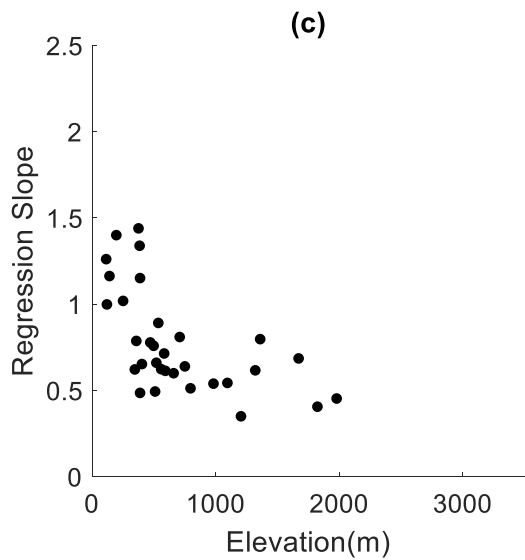
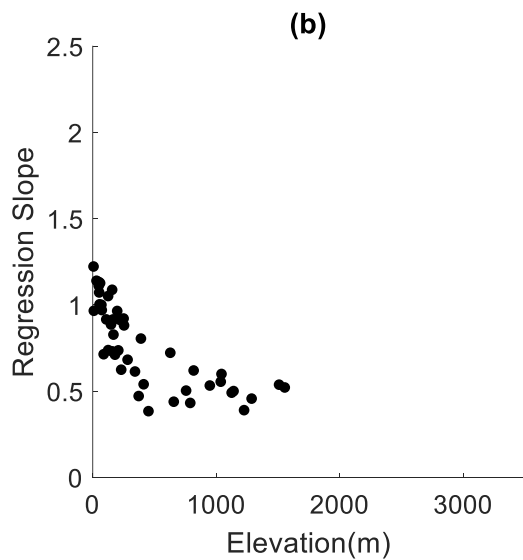
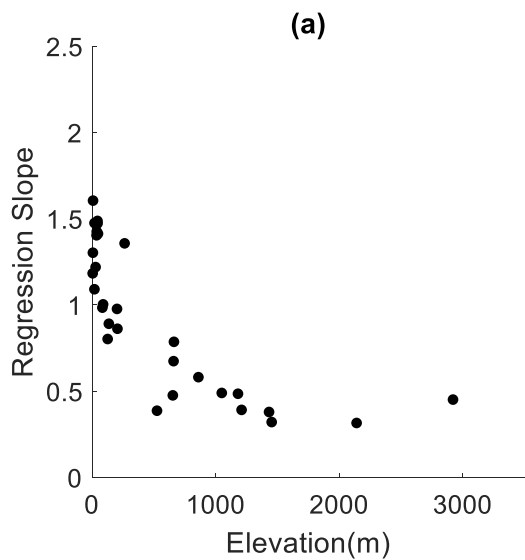
(c)

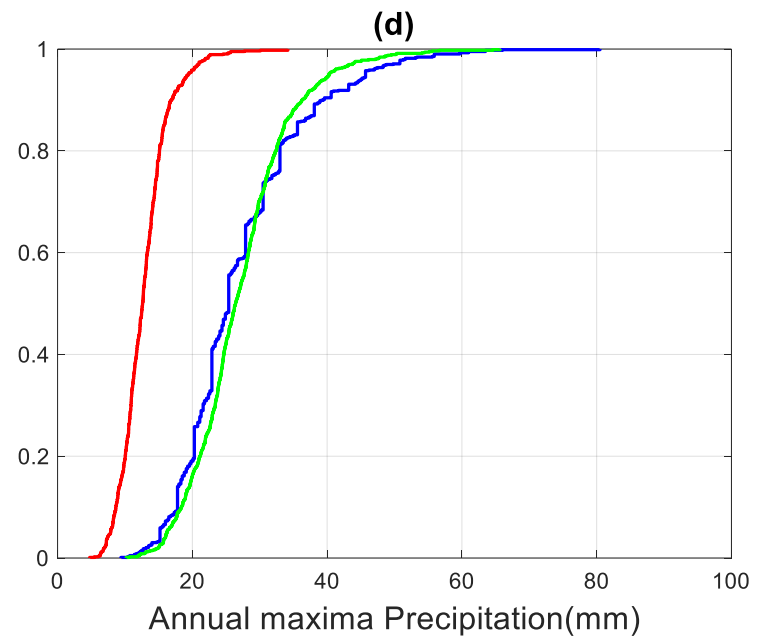
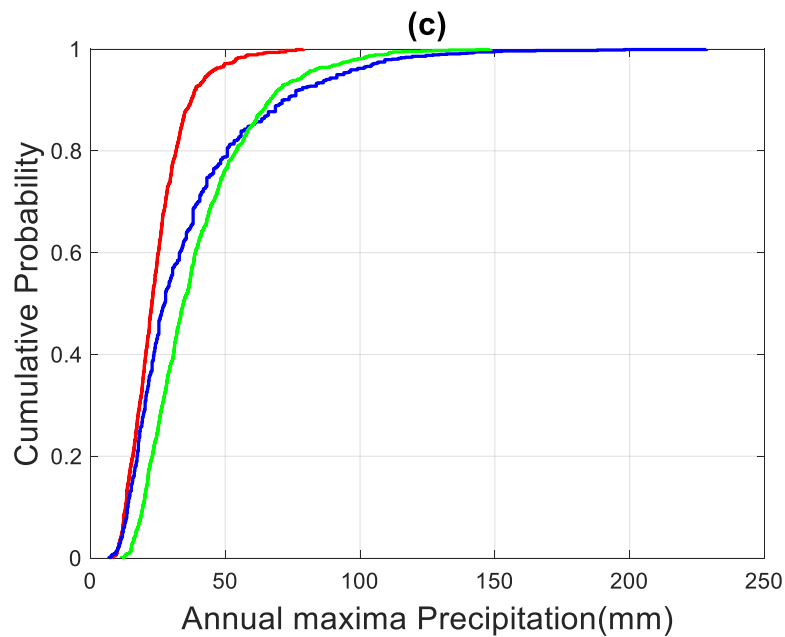
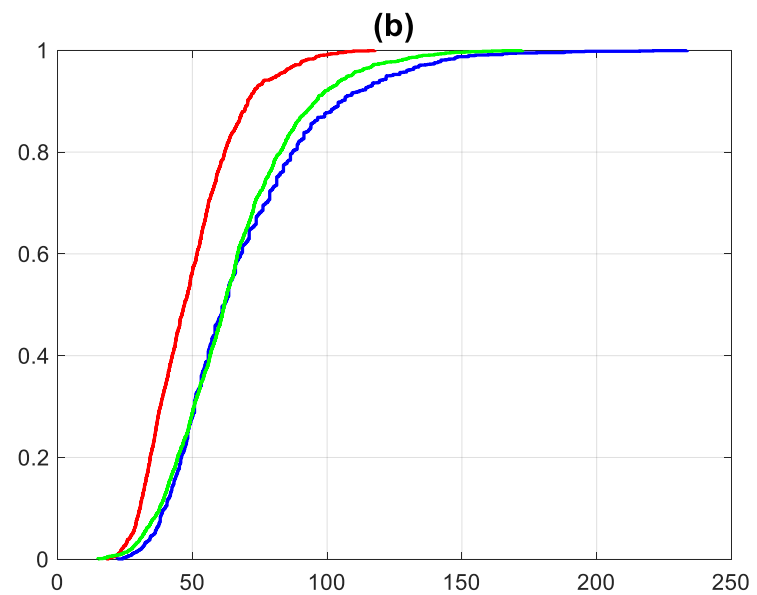
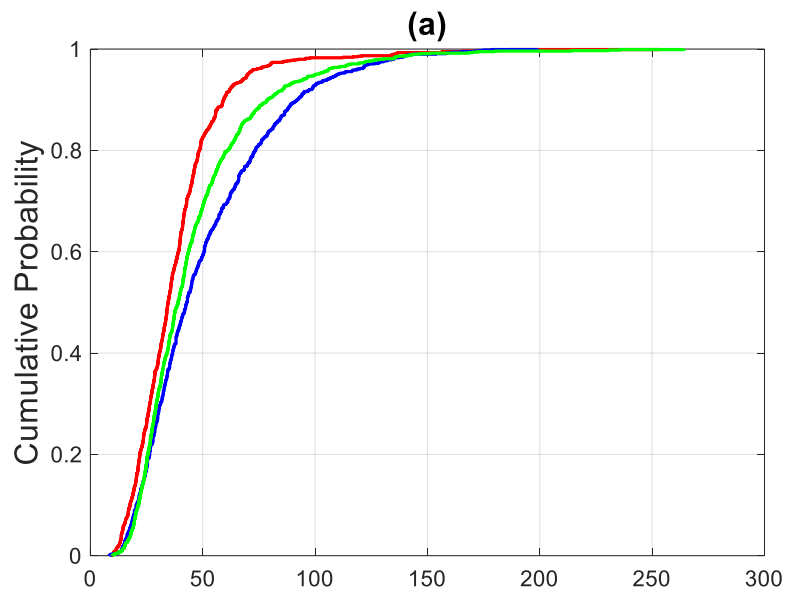


* Annual Maxima Data — Regression Line - - - Reference Line

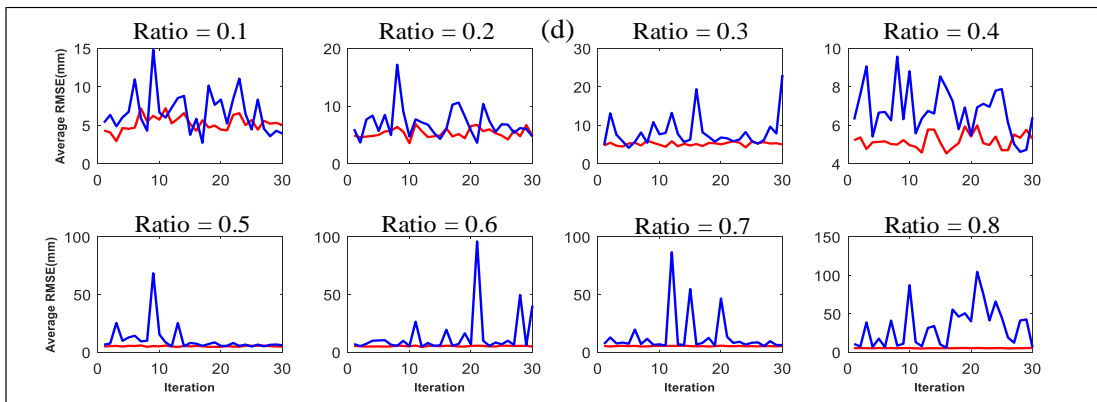
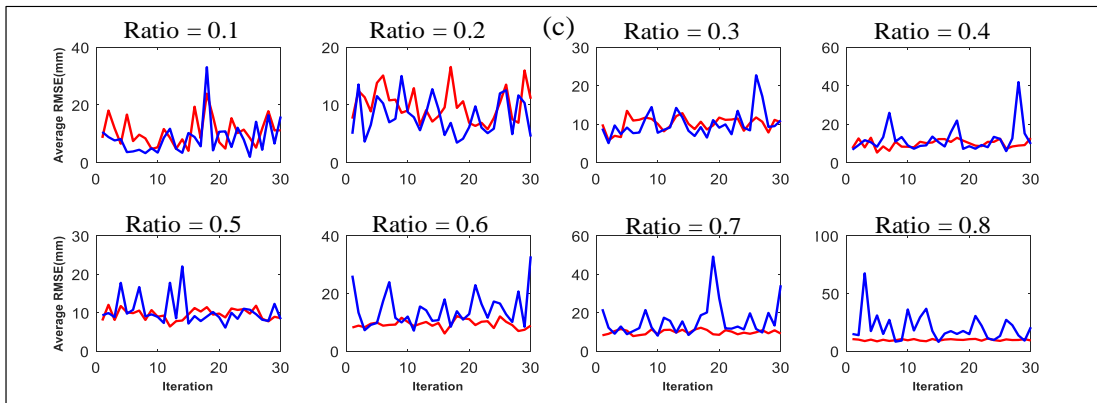
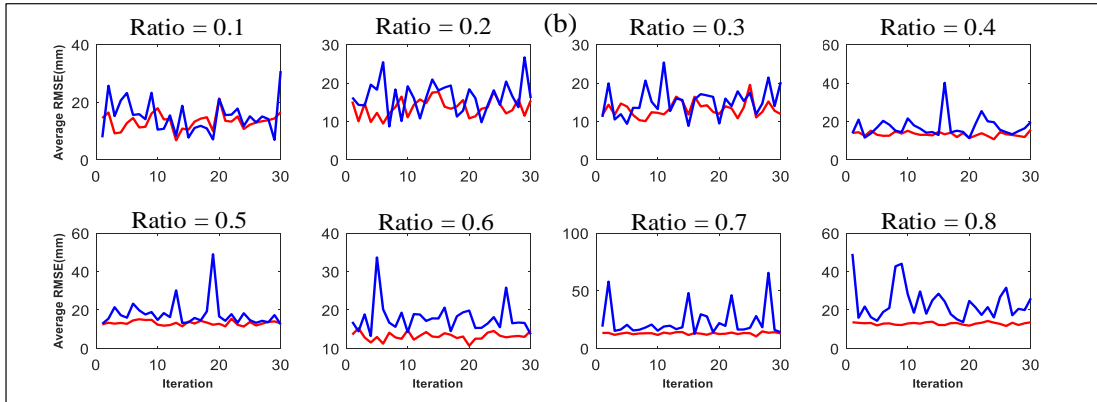
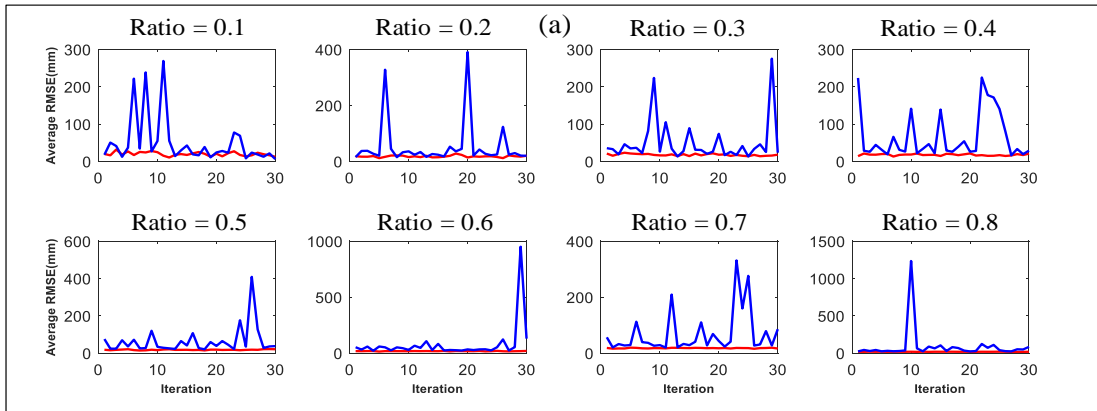


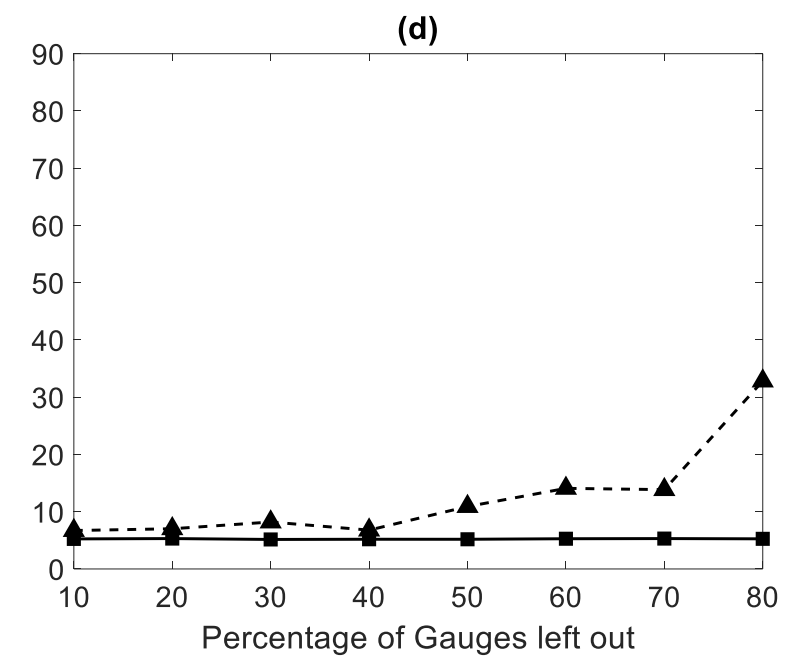
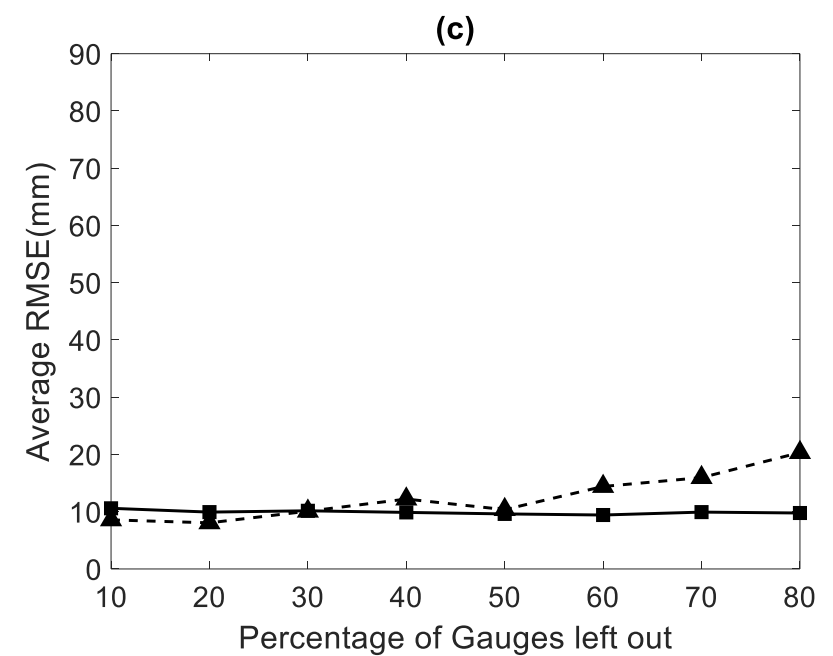
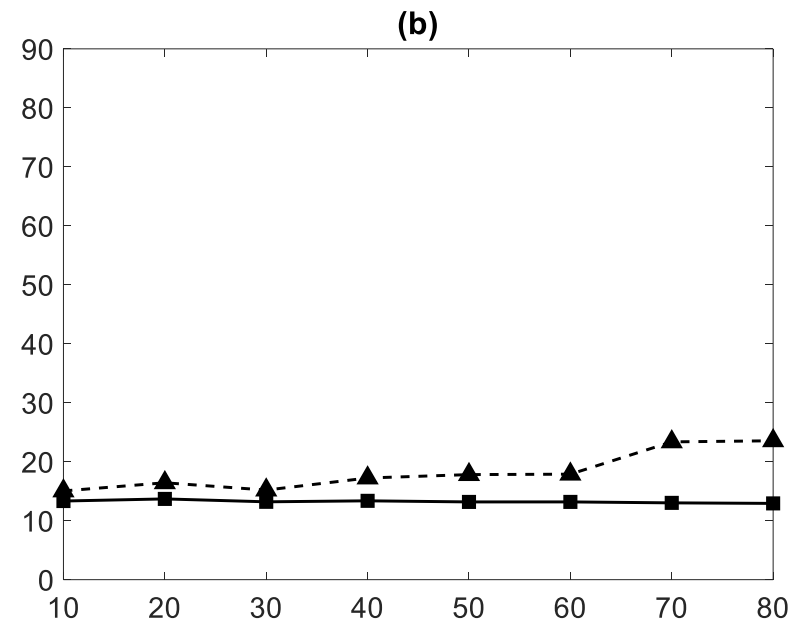
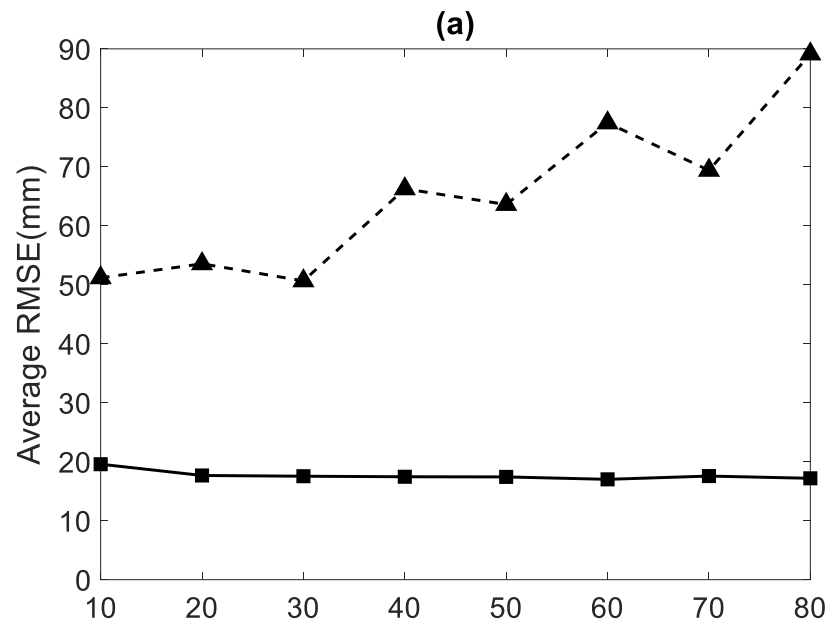
* Annual Maxima Data — Regression Line - - - Reference Line

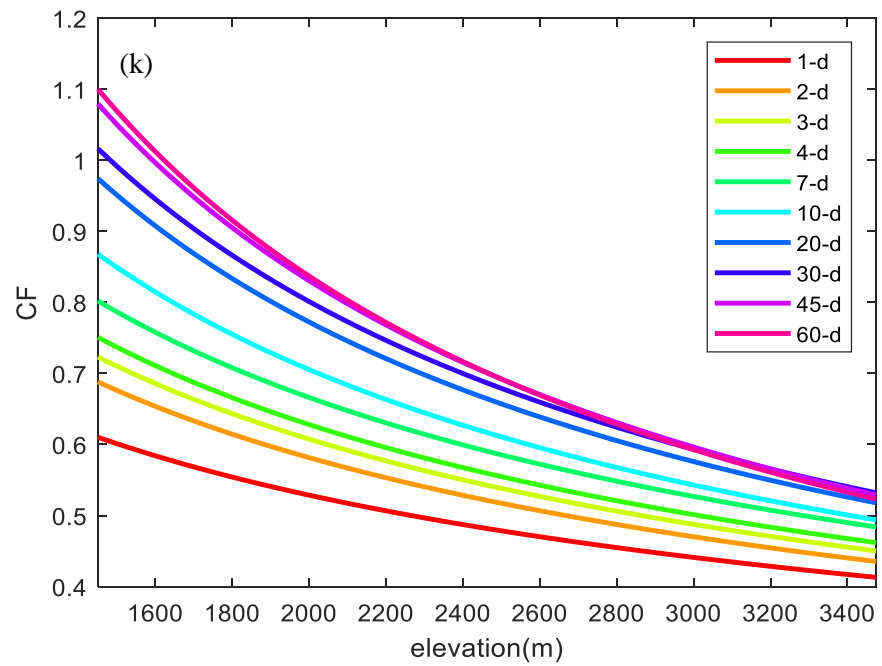
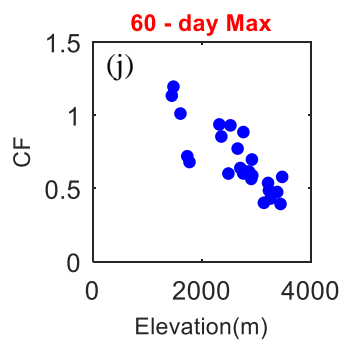
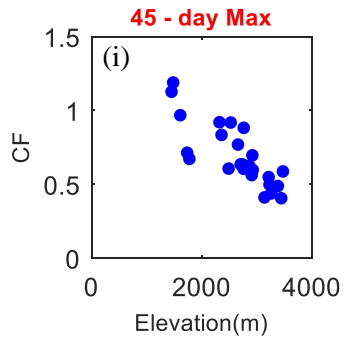
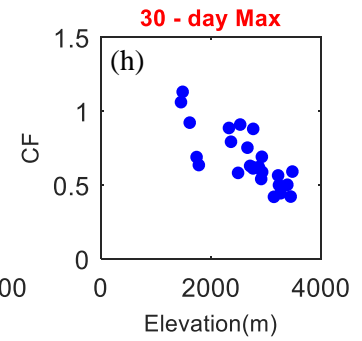
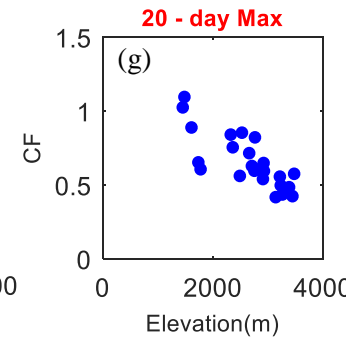
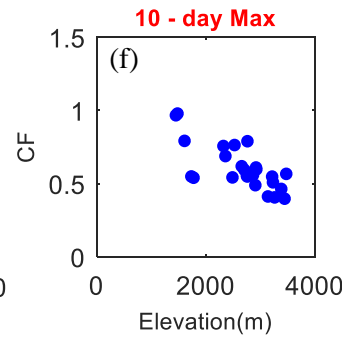
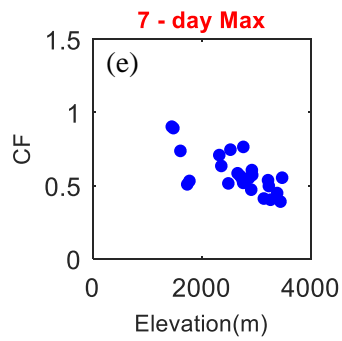
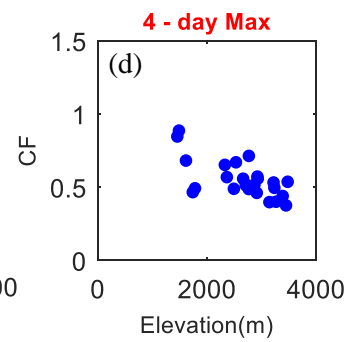
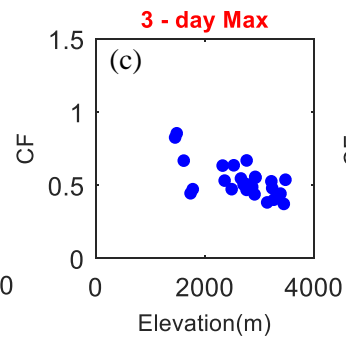
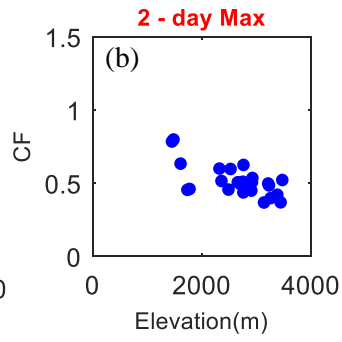
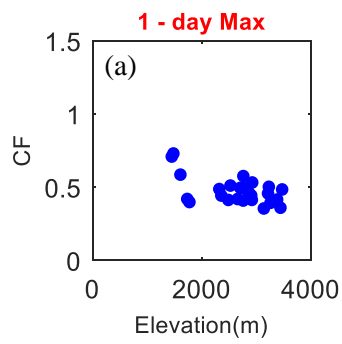


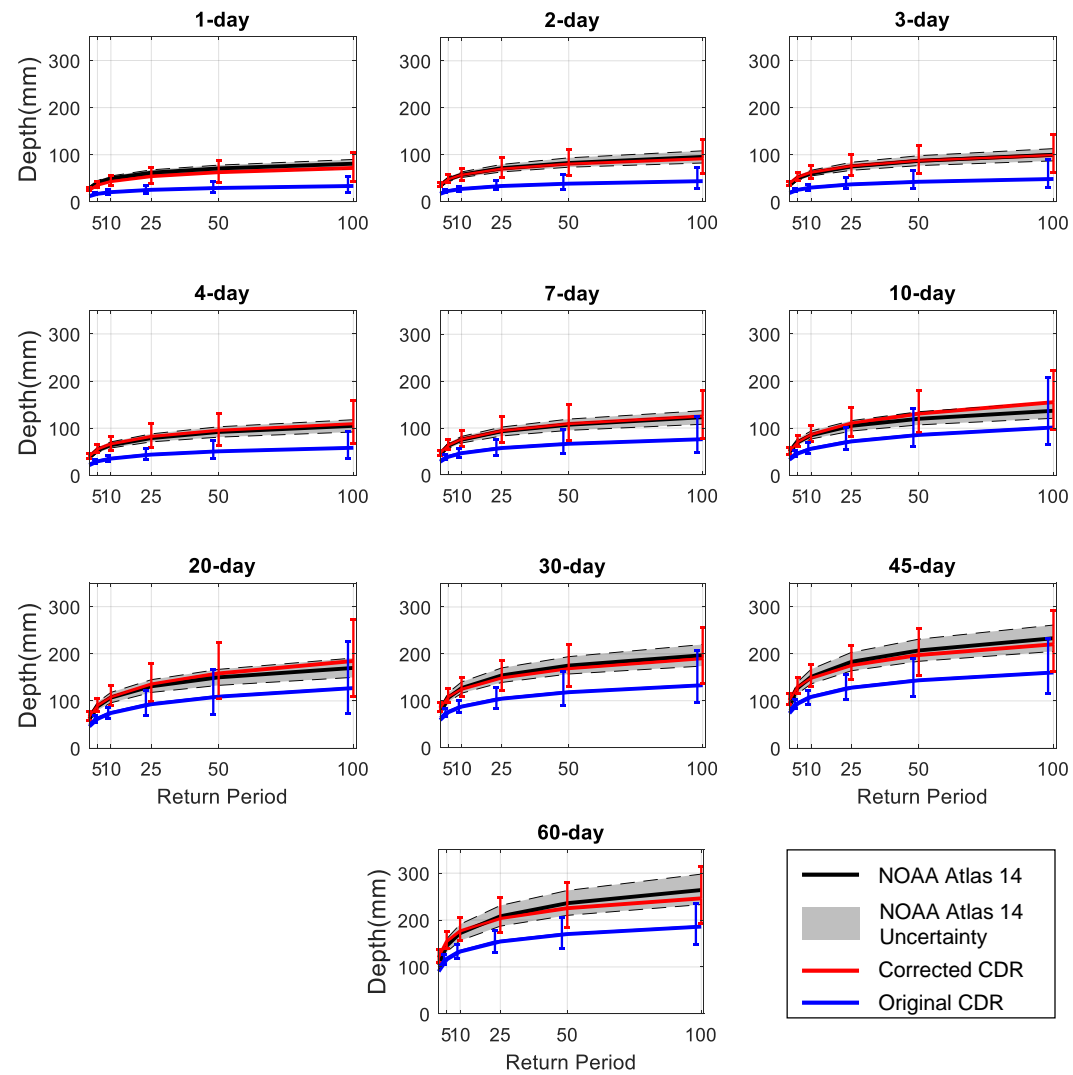


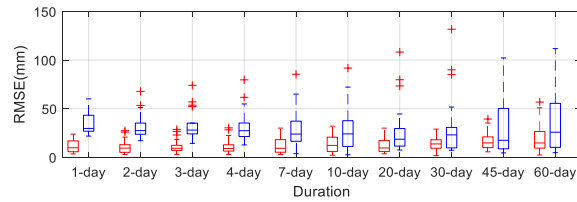
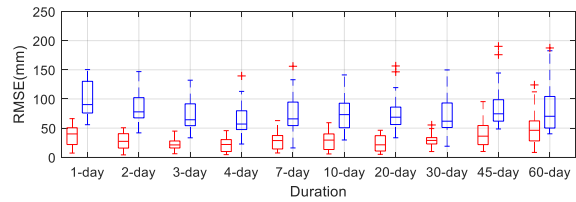
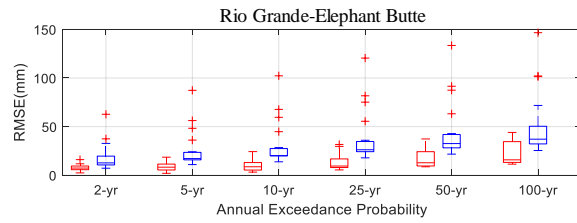
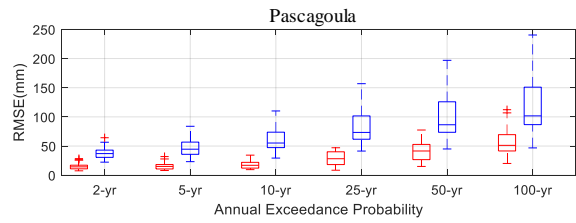
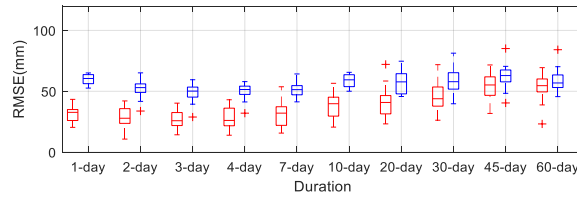
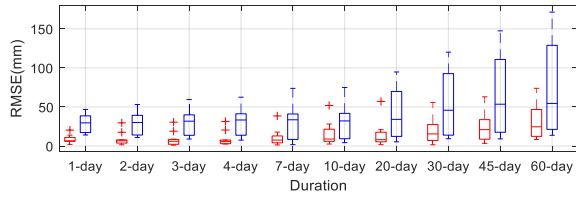
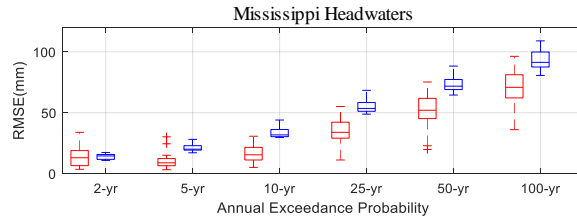
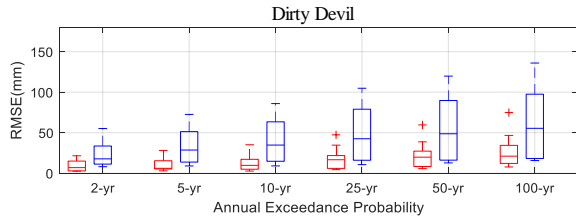
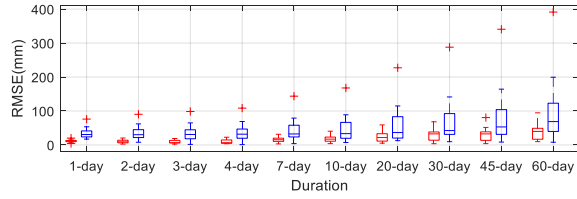
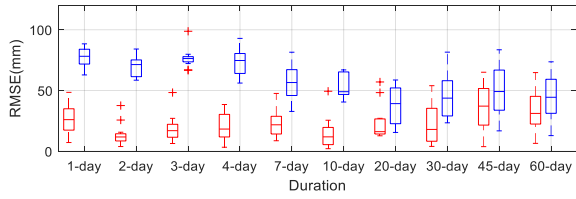
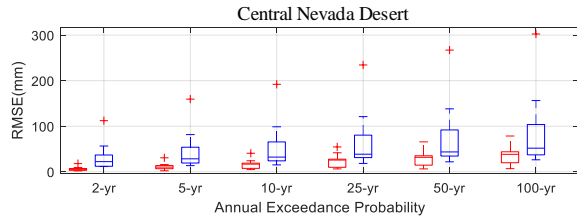
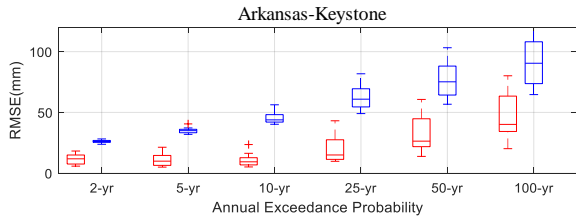
— PERSIANN-CDR — Gauge data — Corrected PERSIANN-CDR



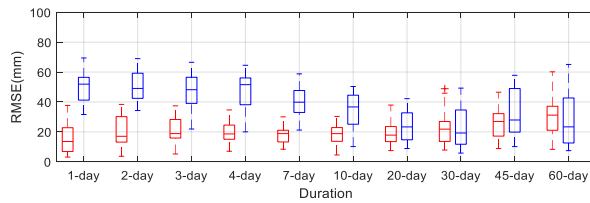
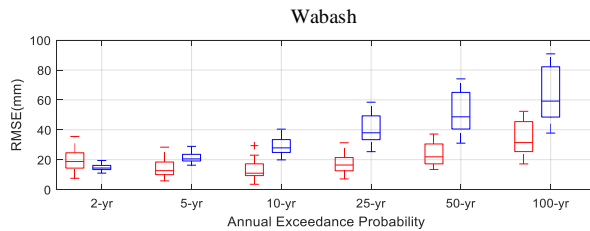
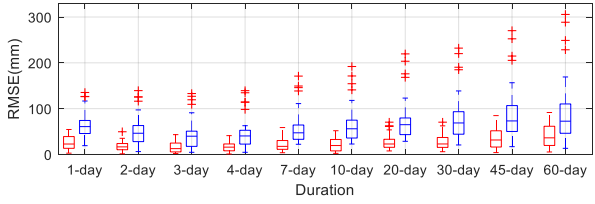
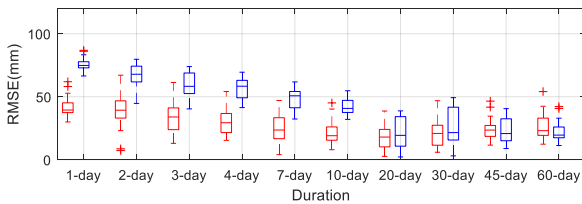
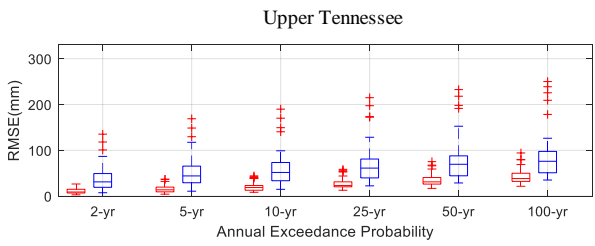
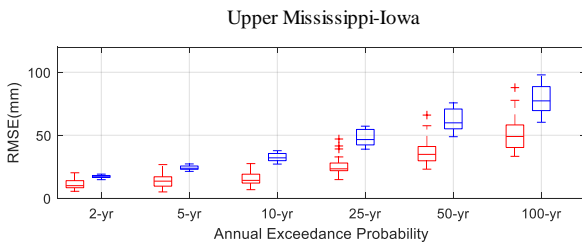
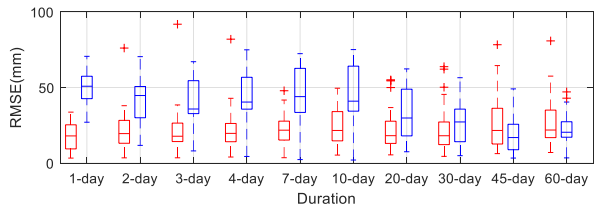
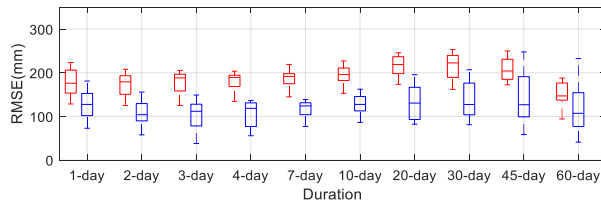
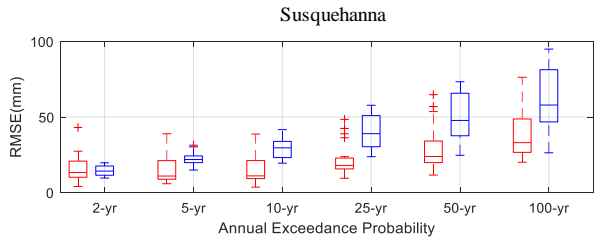
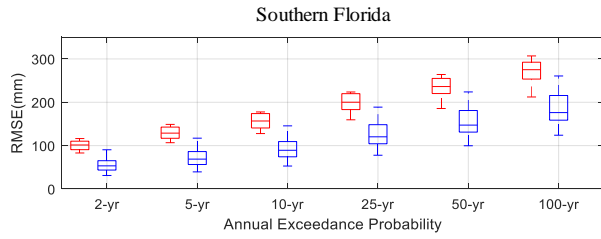




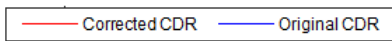
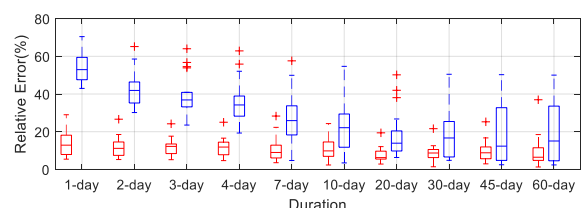
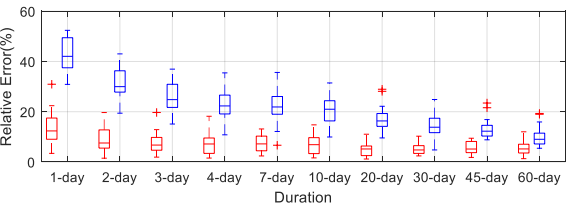
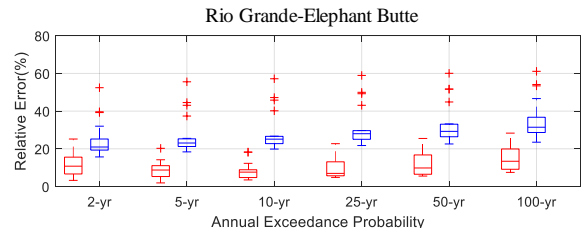
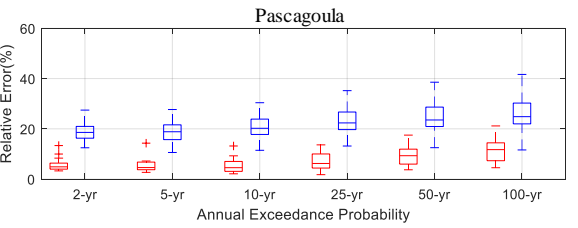
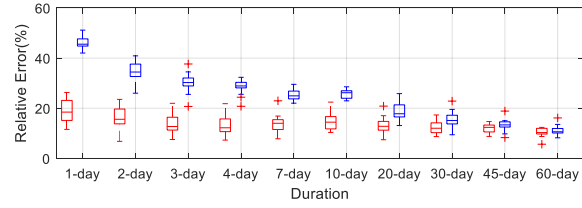
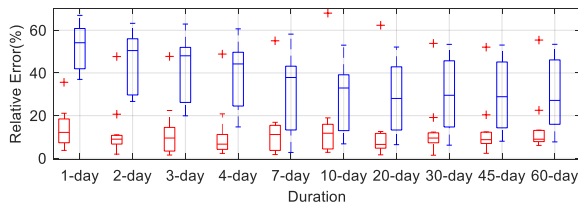
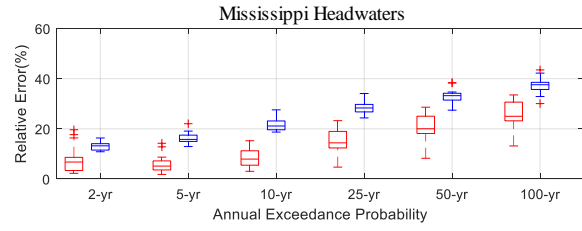
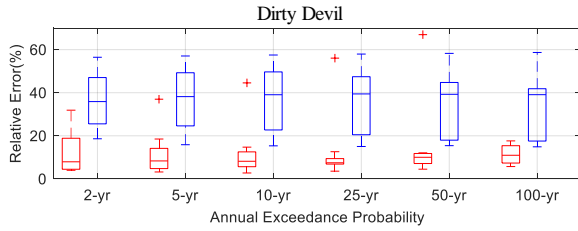
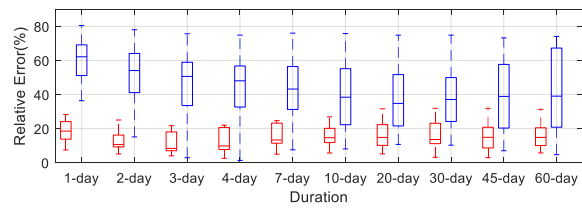
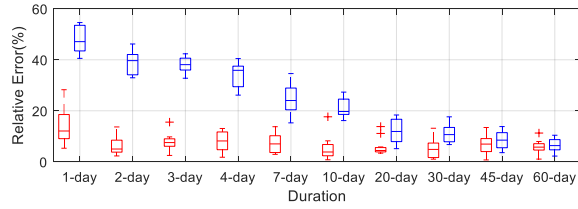
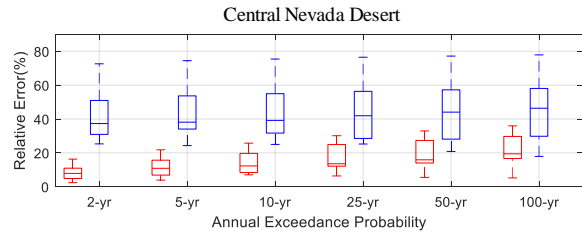
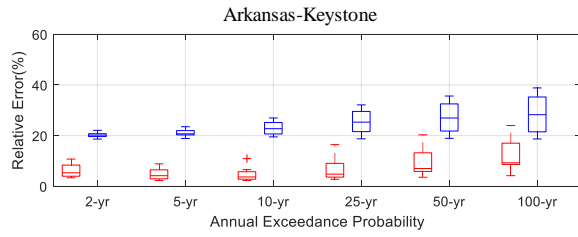


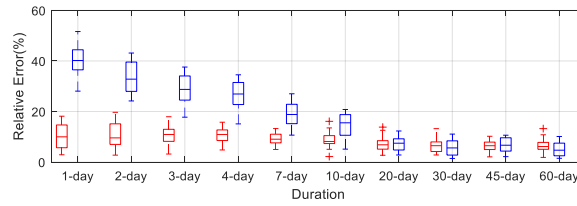
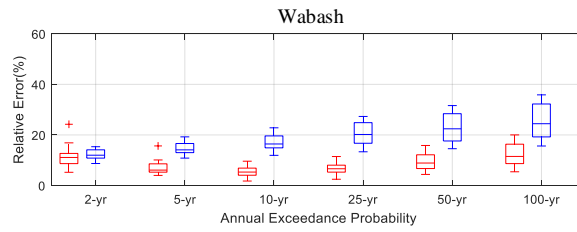
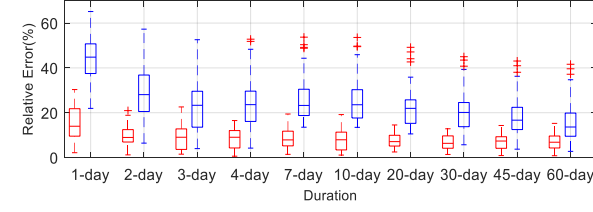
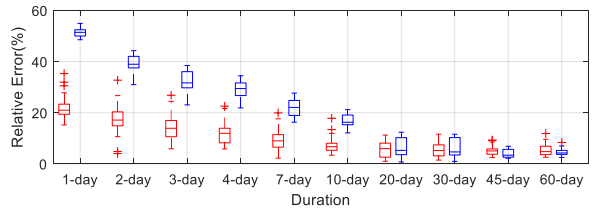
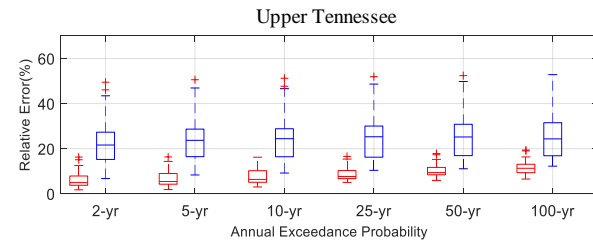
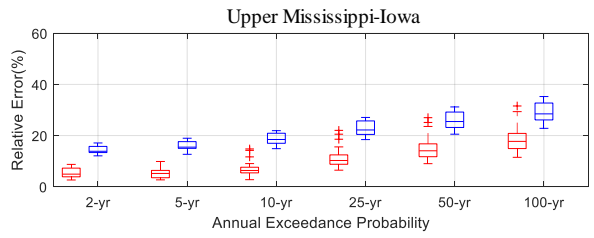
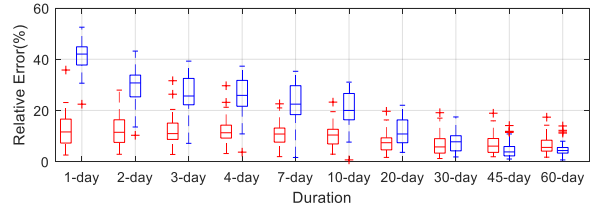
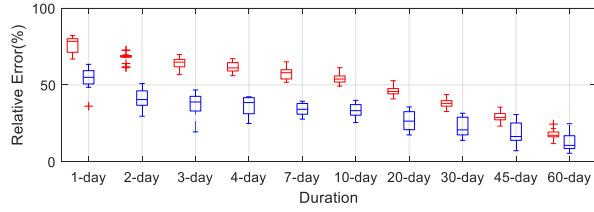
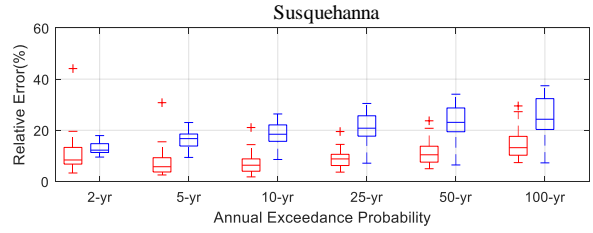
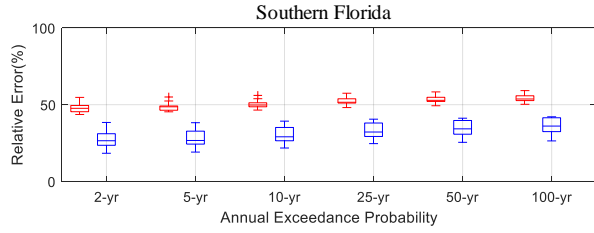


— Corrected CDR — Original CDR



— Corrected CDR — Original CDR





— Corrected CDR — Original CDR

Table 1. Summary of the features of the selected basins and gauges

Basin No.	Basin Name	HUC	State(s)	Area (sq. mi.)	No. of gauges	Gauge elevations (m)			Köppen-Geiger climate class	Climate Description
						Min	Max	Mean		
1	Arkansas-Keystone	1106	KS, OK	9750	12	253.0	454.2	347.7	Dfa, Cfa	Continental, temperate
2	Central Nevada Desert	1606	NV	47100	14	1299.1	2448.5	1818.6	BSk, BWk, BWh, Dfb	Dry, continental
3	Colorado Headwaters	1401	CO	9730	25	1450.8	3474.7	2646.2	BSk, Dfb, Dfc	Dry, continental
4	Dirty Devil	1407	UT, AZ	13500	11	1164.9	2987.0	2093.1	BSk, Bwk, Dfb	Dry, continental
5	Kootenai-Pend Oreille-Spokane	1701	MT, ID, WA	36600	30	548.6	2514.6	1691.5	Dsb, Dfb	Continental
6	Lower Snake	1706	ID, WA, OR	11800	23	328	2788.9	1523.3	Dfb, Dsb	Continental
7	Mississippi Headwaters	0701	MN	20200	19	278.0	454.2	372.2	Dfb	Continental
8	Nueces-Southwestern Texas Coastal	1211	TX	29000	15	43	625.4	217.8	Cfa	Temperate
9	Pascagoula	0317	MS	12100	20	2.4	164.9	72.3	Cfa	Temperate
10	Rio Grande - Elephant Butte	1302	NM	26900	19	1378.9	2621.3	1843.8	Dfb, BSk	Continental, dry
11	San Joaquin	1804	CA	15600	30	3.7	2920	537.2	Csa, BSk	Temperate, dry
12	Southern Florida	0309	FL	18700	14	0.9	10.7	4.3	Cfa, Aw	Temperate, tropical
13	Susquehanna	0205	PA, NY, MD	27200	30	78.9	566.9	313.5	Dfa, Dfb	Continental
14	Trinity	1203	TX	18000	24	103.9	339.9	208.7	Cfa	Temperate
15	Upper Columbia	1702	WA	22600	32	113.1	1978.2	689.3	Dfb, Dsb, BSk	Continental, dry
16	Upper Mississippi-Iowa	0708	IA, IL, MN	22800	25	195.1	390.1	319.0	Dfa, Dfb	Continental
17	Upper Tennessee	0601	TN, NC, GA, VA	17200	28	230.1	1143.9	555.5	Cfa	Temperate
18	Upper Yellowstone	1007	MT, WY	14400	30	944.3	2865.1	1906.2	Dfb, Dfc, BSk	Continental, dry
19	Wabash	0512	IN, IL, OH	32600	26	134.7	284.1	202.2	Dfa	Continental
20	Willamette	1709	OR	11400	46	6.4	1554.5	434.7	Csb, Dsb, Dsc	Temperate, continental

Table 2. The RMSE(mm) of the original and corrected PERSIANN-CDR data during hold-out cross-validation at different gauge locations and basins

San Joaquin		Willamette		Upper Columbia		Colorado Headwaters	
Corrected	Original	Corrected	Original	Corrected	Original	Corrected	Original
14.76	16.74	27.60	54.73	13.30	19.68	6.16	18.20
19.13	34.44	5.78	5.78	3.76	3.09	4.71	18.73
32.66	47.61	11.26	24.65	4.12	8.66	5.44	18.29
31.41	69.29	15.46	11.15	1.32	8.61	5.25	10.88
12.96	<u>4.26</u>	16.73	19.15	2.93	8.02	7.02	9.76
43.12	71.64	30.79	50.90	7.38	31.30	6.43	19.97
9.42	8.59	6.51	9.53	3.61	<u>1.91</u>	8.98	<u>6.50</u>
10.03	10.10	7.42	20.92	15.25	20.72	6.21	17.25
19.79	25.71	11.85	18.53	1.69	4.71	4.12	12.42
6.11	5.49	10.43	11.36	4.97	8.45	4.80	16.22
19.16	36.62	4.99	<u>4.21</u>	6.20	10.88	5.09	12.83
30.47	59.50	6.65	11.81	0.96	4.25	3.74	18.69
8.86	13.73	20.38	37.86	9.12	21.90	4.74	12.75
23.12	<u>10.42</u>	9.43	<u>7.62</u>	3.17	4.97	4.03	19.37
6.57	6.29	14.50	21.04	11.72	<u>6.27</u>	2.61	18.97
16.38	19.47	9.79	19.52	7.36	15.71	5.66	23.01
30.53	20.49	13.75	<u>8.71</u>	0.92	4.30	1.98	15.97
3.25	9.45	13.34	40.60	5.08	9.13	4.12	13.03
22.05	50.93	45.06	65.65	26.64	34.04	5.98	14.10
8.12	26.77	11.12	11.52	8.59	9.39	4.32	13.81
13.91	18.23	2.94	4.90	3.58	10.14	2.73	15.47
13.69	23.67	2.36	6.02	8.59	<u>4.84</u>	3.01	15.38
10.34	15.72	17.35	7.06	19.52	<u>8.05</u>	6.20	12.17
17.74	36.22	4.41	8.65	7.33	40.04	7.29	23.12
24.67	47.21	24.83	44.44	14.55	53.51	9.89	<u>5.98</u>
19.90	31.57	11.39	<u>4.63</u>	9.88	19.40	-	-
12.03	27.90	9.58	27.84	8.47	28.97	-	-
16.77	20.93	3.29	3.55	19.66	<u>14.44</u>	-	-
-	-	6.39	33.06	43.31	77.52	-	-
-	-	7.81	27.53	13.28	<u>7.61</u>	-	-
-	-	25.35	54.10	17.14	<u>10.74</u>	-	-
-	-	8.42	39.02	-	-	-	-
-	-	9.66	44.36	-	-	-	-
-	-	29.91	66.88	-	-	-	-
-	-	11.66	37.27	-	-	-	-
-	-	13.56	48.13	-	-	-	-
-	-	7.22	24.98	-	-	-	-
-	-	6.97	34.96	-	-	-	-
-	-	13.64	56.23	-	-	-	-
-	-	16.40	24.77	-	-	-	-
-	-	4.53	6.53	-	-	-	-
-	-	12.97	<u>10.91</u>	-	-	-	-
-	-	5.74	7.32	-	-	-	-

Note: The underlined values show the cases where the RMSE of the original PERSIANN-CDR is lower than that of corrected PERSIANN-CDR.

Table 3. The RMSE (mm) from leave one out cross validation using gauge interpolation, original and corrected PERSIANN-CDR data

Method	Basin Name			
	San Joaquin	Willamette	Upper Columbia	Colorado Headwaters
Interpolation	21.61	16.06	7.87	6.84
Corrected CDR	17.34	12.77	<u>9.79</u>	5.22
Original CDR	26.45	23.95	16.22	15.31

Note: The underlined value shows the case where the corrected PERSIANN-CDR method gave a higher RMSE value at basin scale than the interpolation method.

Table 4. Bias-correction results in selected basins over the United States

Basin No.	Basin Name	Average RMSE(mm)		Change (%)
		Original PERSIANN-CDR	Corrected PERSIANN-CDR	
1	Arkansas-Keystone	30.90	12.02	-61.1
2	Central Nevada Desert	14.16	6.91	-51.2
4	Dirty Devil	15.35	3.27	-78.7
5	Kootenai-Pend Oreille-Spokane	24.23	9.67	-60.1
6	Lower Snake	17.36	4.94	-71.6
7	Mississippi Headwaters	19.12	3.42	-82.1
8	Nueces-Southwestern Texas Coastal	28.68	17.43	-39.2
9	Pascagoula	39.20	36.32	-7.3
10	Rio Grande - Elephant Butte	15.67	4.34	-72.3
12	Southern Florida	35.40	45.92	<u>+29.7</u>
13	Susquehanna	22.61	10.64	-52.9
14	Trinity	35.62	21.87	-38.6
16	Upper Mississippi-Iowa	23.83	7.24	-69.6
17	Upper Tennessee	27.14	10.15	-62.6
18	Upper Yellowstone	18.68	5.31	-71.6
19	Wabash	23.36	11.46	-51.0

Note: The underlined value shows the case where the adjustment failed to improve the errors.